JGR Solid Earth

RESEARCH ARTICLE
10.1029/2021JB021895

Decrypting Magnetic Fabrics (AMS, AARM, AIRM) Through the Analysis of Mineral Shape Fabrics and Distribution Anisotropy

Tobias Mattsson[1,2,3], Benoît Petri[4], Bjarne Almqvist[3], William McCarthy[2], Steffi Burchardt[3], J. Octavio Palma[5,6], Øyvind Hammer[7], and Olivier Galland[8]

[1]Department of Geological Sciences, Stockholm University, Stockholm, Sweden, [2]School of Earth and Environmental Sciences, University of St. Andrews, UK, [3]Department of Earth Sciences, Uppsala University, Uppsala, Sweden, [4]Université de Strasbourg, CNRS, ITES UMR 7063, Strasbourg, France, [5]Subsecretaría de Minería Provincia de Buenos Aires, Argentina, [6]Facultad de Ciencias Naturales y Museo, Unviersidad Nacional de La Plata, Buenos Aires, Argentina, [7]Natural History Museum, University of Oslo, Oslo, Norway, [8]Department of Geosciences, Physics of Geological Processes, The NJORD Centre, University of Oslo, Oslo, Norway

Key Points:

- Trachyandesite analyzed with X-ray microtomography for comparison between magnetic fabrics and the components of the petrofabric
- Magnetite and amphibole shape fabrics and magnetite distribution constructively or destructively interfere to produce magnetic fabrics
- Distribution anisotropy significantly affects the anisotropy of magnetic susceptibility and anisotropy of remanent magnetization

Supporting Information:

Supporting Information may be found in the online version of this article.

Correspondence to:

T. Mattsson,
tobias.mattsson@geo.su.se

Citation:

Mattsson, T., Petri, B., Almqvist, B., McCarthy, W., Burchardt, S., Palma, J. O., et al. (2021). Decrypting magnetic fabrics (AMS, AARM, AIRM) through the analysis of mineral shape fabrics and distribution anisotropy. *Journal of Geophysical Research: Solid Earth*, *126*, e2021JB021895. https://doi.org/10.1029/2021JB021895

Received 16 FEB 2021
Accepted 23 MAY 2021

Abstract Anisotropy of magnetic susceptibility (AMS) and anisotropy of magnetic remanence (AARM and AIRM) are efficient and versatile techniques to indirectly determine rock fabrics. Yet, deciphering the source of a magnetic fabric remains a crucial and challenging step, notably in the presence of ferrimagnetic phases. Here we use X-ray micro-computed tomography to directly compare mineral shape-preferred orientation and spatial distribution fabrics to AMS, AARM and AIRM fabrics from five hypabyssal trachyandesite samples. Magnetite grains in the trachyandesite are euhedral with a mean aspect ratio of 1.44 (0.24 s.d., long/short axis), and >50% of the magnetite grains occur in clusters, and they are therefore prone to interact magnetically. Amphibole grains are prolate with magnetite in breakdown rims. We identified three components of the petrofabric that influence the AMS of the analyzed samples: The magnetite and the amphibole shape fabrics and the magnetite distribution anisotropy. Depending on their relative strength, orientation and shape, these three components interfere either constructively or destructively to produce the AMS fabric. If the three components are coaxial, the result is a relatively strongly anisotropic AMS fabric ($P' = 1.079$). If shape fabrics and/or magnetite distribution anisotropy are non-coaxial, the resulting AMS is weakly anisotropic ($P' = 1.012$). This study thus reports quantitative petrofabric data that show the effect of magnetite distribution anisotropy on magnetic fabrics in igneous rocks, which has so far only been predicted by experimental and theoretical models. Our results have first-order implications for the interpretation of petrofabrics using magnetic methods.

1. Introduction

The analysis of magnetic fabrics by means of anisotropy of magnetic susceptibility (AMS) and anisotropy of anhysteretic and isothermal remanence magnetization (AARM and AIRM) are routinely employed for rock fabric (or petrofabric) determination. Their use is highly versatile, from the analysis of igneous flow fabrics in intrusive and extrusive environments (Cañón-Tapia & Castro, 2004; Chadima et al., 2009; Eriksson et al., 2011; Geoffroy et al., 2002; Khan, 1962; Knight & Walker, 1988; Martin et al., 2019; Mattsson et al., 2018; McCarthy et al., 2015a; Stevenson et al., 2007; Tauxe et al., 1998) and magmatic to sub-magmatic state tectonic overprinting (Di Chiara et al., 2020; McCarthy et al., 2015b; Petronis et al., 2012), to solid-state deformation fabrics across low-grade (Cifelli et al., 2009; García-Lasanta et al., 2013), to high-grade metamorphic conditions (Borradaile & Lagroix, 2001; Merz et al., 2019). To reliably interpret magma flow or rock deformation from AMS data require knowing a crucial intermediate step: The relationship between the magnetic signal and the petrofabric. However, constraining which minerals give rise to the magnetic fabric, and how the shape and spatial arrangement of these minerals impact magnetic anisotropy, remains challenging (Biedermann, 2020a; Borradaile & Jackson, 2010).

The source of the AMS of a rock is principally the shape and the crystallographic preferred orientations of mineral grains (SPO and CPO, respectively), and the magnetic interaction between ferro- and ferrimagnetic particles (Biedermann, 2018; Borradaile & Jackson, 2010; Bouchez, 2000; Butler & Banerjee, 1975; Frandsen

et al., 2004; Schöpa et al., 2015). For paramagnetic minerals such as pyroxene, amphibole, and biotite, the AMS principal axes usually correlates to crystallographic axes and are produced by the Fe spatial ordering in the crystal lattice (Biedermann, 2018; Biedermann et al., 2015; Borradaile & Jackson, 2010). However, this relation does not hold for ferrimagnetic minerals (in particular magnetite) because the (low-field) AMS may have several sources, in this case domain state and distribution anisotropy (DA) are two key factors (Ferré, 2002; Hrouda, 1982; Potter & Stephenson, 1988; Stephenson et al., 1986).

The grain-scale AMS of ferrimagnetic minerals is known to be dependent on domain state: In multi-domain (MD) magnetite, the axes of the AMS ellipsoid (k_1, k_2, k_3) correlate with the long (v_1), intermediate (v_2) and short (v_3) axes of the magnetite crystal (Borradaile & Jackson, 2010; Dunlop, 1981; Ferré, 2002; Hrouda, 1982); while for single-domain (SD) magnetite grains, the AMS axes inversely correlate with the grain shape (k_1 coaxial to v_3 and k_3 coaxial to v_1), leading to so-called inverse magnetic fabrics (Almqvist et al., 2012; Ferré, 2002; Potter & Stephenson, 1988; Rochette et al., 1992, 1999; Stephenson et al., 1986).

DA is caused by the magnetic interaction of closely spaced ferri and ferromagnetic grains (e.g., magnetite, pyrrhotite), this phenomenon may also be reflected in the AMS fabric (Cañón-Tapia, 1996; Gaillot et al., 2006; Grégoire et al., 1995, 1998; Hargraves et al., 1991; Stephenson, 1994). For example, a planar AMS fabric may be observed when magnetite grains are distributed in planes such as in magmatic cumulate layers (Hargraves et al., 1991; Selkin et al., 2014), even if individual magnetite grains are aligned along a single axis that defines a linear SPO. However, for DA to become significant, ferrimagnetic minerals need to be closely clustered since their interaction weakens exponentially with the distance between crystals (Stephenson, 1994). Gaillot et al. (2006) defined a ratio between mean crystal grain size (d) and distance between crystal centers (r) that predicts that weak ferrimagnetic grain–grain interaction occurs when (d/r) > 0.5 and strong grain–grain interaction will occur when (d/r) > 0.8. They further proposed that DA is not a significant contributor to AMS unless the magnetic mineralogy of a sample is dominated by ferrimagnetic minerals with very low shape anisotropy (Gaillot et al., 2006).

One way to investigate the source of the AMS fabric is by cross referencing data arising from multiple magnetic anisotropy methods and petrofabric analysis. AARM is controlled by magnetic remanence and is used to measure the fabric of ferrimagnetic minerals in isolation from other rock forming minerals that may bias the AMS of a sample (Bilardello & Jackson, 2014; Borradaile & Jackson, 2010; Jackson, 1991; McCabe et al., 1985). Low-field AIRM can further be applied to identify the contribution of low-coercivity grains, such as MD titanomagnetite and MD magnetite, to the AMS fabric (Bogue et al., 1995; Stephenson et al., 1986; Tarling & Hrouda, 1993). Mineral SPO studies on ferrimagnetic and silicate minerals using image analysis have commonly been used to decrypt the source of the magnetic fabrics (Arbaret et al., 2013; Archanjo & Launeau, 2004; Geoffroy et al., 2002; Launeau & Cruden, 1998; Payacán et al., 2014; Petronis et al., 2004; Schöpa et al., 2015). SPO analyses have also been conducted using high-resolution X-ray micro-computed tomography imaging (μXCT), which offers the opportunity to obtain 3D grain shape and location data on the same sample as analyzed with AMS (Schöpa et al., 2015; Zhu et al., 2017). However, unlike experimental and theoretical approaches (Biedermann, 2019, 2020b; Gaillot et al., 2006; Grégoire et al., 1995; Hargraves et al., 1991; Stephenson, 1994), petrofabric studies on natural rocks have so far not been able to show a close relationship between DA and the AMS ellipsoid axes orientation and shape. The large center to center spacing that occurs between ferrimagnetic grains in many rock types likely rendered magnetic interactions largely negligible (Grégoire et al., 1998; Schöpa et al., 2015). The contribution of DA to the AMS fabric of a sample has therefore not been fully assessed.

Here we address the contribution of DA to magnetic fabrics in natural samples by directly comparing AMS, AARM and AIRM data to SPO and DA data generated using a newly developed statistical approach to quantify petrofabrics of μXCT mineral data (Petri et al., 2020). We present a detailed analysis of the petrofabric of a hypabyssal trachyandesite from the Chachahuén volcano, Argentina (cf. Burchardt et al., 2019). In the trachyandesite, over 50% of ferrimagnetic oxides occur in clusters (see below), this petrographic relationship allows us to directly investigate ferrimagnetic DA in comparison to AMS, AARM and AIRM data.

1.1. The Cerro Bayo Cryptodome

The analyzed samples were collected from the Cerro Bayo cryptodome, which has a volume of >0.3 km^3 and formed at 6.7 ± 0.3 Ma in the Chachahuén volcanic system, Argentina (Figure S1) (Burchardt et al., 2019; Holm-

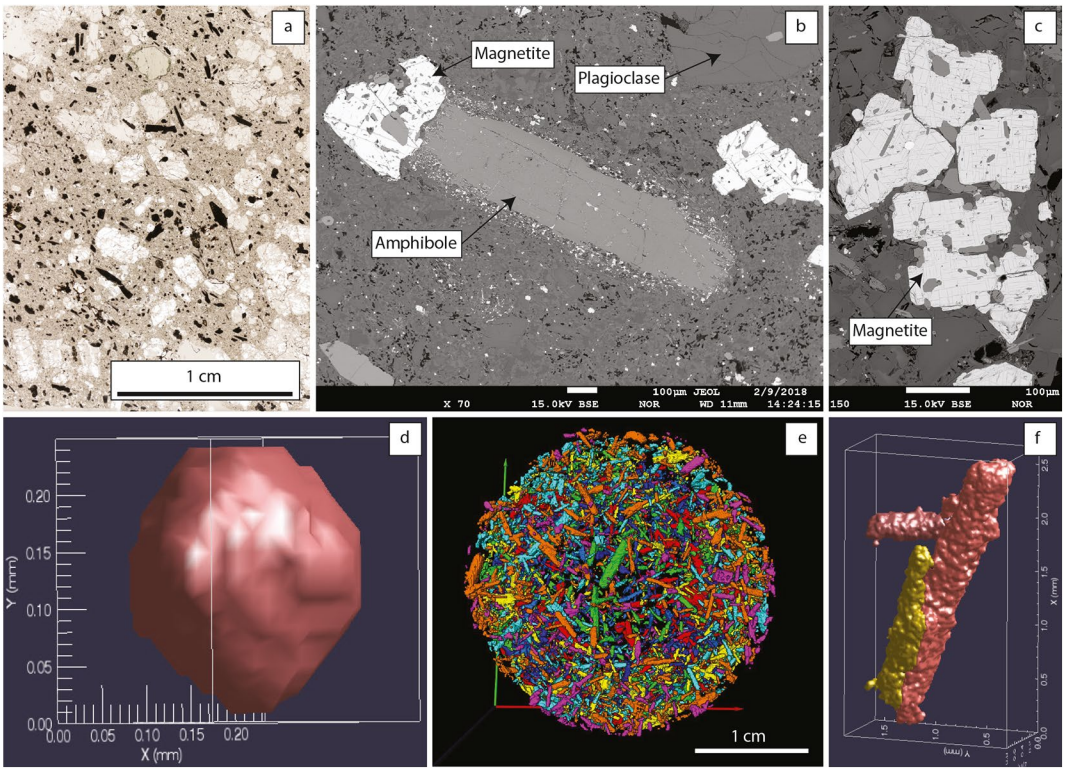

Figure 1. (a) Plane-polarized microphotograph of plagioclase- (light crystals) and amphibole- (dark and green crystals) phyric Cerro Bayo trachyandesite. (b) Back-scattered electron image of amphibole and magnetite phenocrysts in Cerro Bayo trachyandesite. Note that the breakdown rims on the amphibole consist of small magnetite and pyroxene crystals. (c) Back-scattered electron image of magnetite cluster in Cerro Bayo trachyandesite. (d) Magnetite crystal extracted with Blob3D. The magnetite crystals in Cerro Bayo generally have cubic habits. (e) Amphibole crystals extracted with Avizo from sample CB-55. The crystals are colored to distinguish different crystals. (f) Three prolate amphibole crystals from sample CB-55 separated with Blob3D.

berg, 1962; Kay et al., 2006; Pérez & Condat, 1996). The cryptodome consists of a porphyritic trachyandesite with amphibole and plagioclase phenocrysts and accessory phenocrysts of titanomagnetite and clinopyroxene (Figures 1a–1c) (Burchardt et al., 2019). The amphibole phenocrysts are surrounded by breakdown rims that range from 10 to 100 μm in thickness and consist of small (μm in diameter) crystals of titanomagnetite, pyroxene and feldspar (Figure 1b). Several amphibole crystals also have oxide inclusions, whereas oxide inclusions are rare in the plagioclase phenocrysts. The groundmass is rhyolitic in composition and comprises euhedral to subhedral plagioclase and alkali feldspar laths, euhedral to subhedral apatite and pyroxene, and anhedral quartz (Figure 1a). Plagioclase phenocrysts constitute about 24 vol. % of the rock, amphibole phenocrysts only about 3–7 vol. %, and magnetite and pyroxene phenocrysts constitute ~0.5 vol. % and <<1 vol. % of the rock, respectively. Plagioclase phenocrysts in the Cerro Bayo occur in glomerocrysts or as individual "free-floating" crystals oriented largely parallel to the amphibole shape-preferred orientation (Figure 1a). The dominant iron oxide in the Cerro Bayo trachyandesite has been determined to be titanomagnetite with on average 3.5 wt. % TiO_2 and the amphibole phenocrysts have been classified as pargasite and hastingsite (Sun, 2018). Interpretations of magma flow in the Cerro Bayo cryptodome utilizing the AMS data in this study are presented in Burchardt et al. (2019).

2. Methods

2.1. Magnetic Fabric Analyses

2.1.1. Anisotropy of Magnetic Susceptibility and Thermomagnetic Properties

Five representative, oriented block samples (CB-15, CB-19, CB-46, CB-55 and CB-61) were collected from the Cerro Bayo cryptodome and cored to extract 5, 5, 6, 11 and 6 (21 × 24 mm cylinder) specimens, re-

spectively. AMS measurements were performed in the Laboratory for Experimental Paleomagnetism at the Department of Earth Sciences, Uppsala University with an Agico Kappabridge MFK1-FA in semi-automatic spinning mode. A field of 200 A/m and frequency of 976 Hz were used for the measurements. Symmetric second rank magnetic susceptibility tensors were determined from the measurements using the least square inversion method of Jelínek and Kropáček (1978). The eigenvalues and eigenvectors of the magnetic susceptibility tensor define the value and orientation of the three orthogonal, principal axes of susceptibility, $k_1 \geq k_2 \geq k_3$, which can be represented by a triaxial ellipsoid (the magnetic susceptibility ellipsoid) (Khan, 1962). The mean magnetic susceptibility (K_m) is given by the arithmetic mean of the principal susceptibilities:

$$K_m = \frac{k_1 + k_2 + k_3}{3}$$

The AMS in a rock can be further described by the anisotropy parameter P' (or P_j), and the shape parameter T, as originally defined by Jelínek (1981) and calculated with the software Anisoft5 (Chadima et al., 2019). The corrected degree of anisotropy is defined as:

$$P' = \exp\sqrt{2\left(\left(\eta_1 - \eta_m\right)^2 + \left(\eta_2 - \eta_m\right)^2 + \left(\eta_3 - \eta_m\right)^2\right)}$$

where $\eta_x = ln(k_x), x = 1,2,3$ and $\eta_m = \frac{\eta_1 + \eta_2 + \eta_3}{3}$. The shape factor ($T$) describes the shape of the ellipsoid and is given by:

$$T = \frac{2\eta_2 - \eta_1 - \eta_3}{\eta_1 - \eta_3}$$

The ellipsoid shape can range from rotational oblate ($T = 1$) to rotational prolate ($T = -1$) or triaxial neutral ($T \approx 0$).

The thermomagnetic properties of the samples were determined by measuring the bulk magnetic susceptibility on whole-rock powders of the five sample in three steps using the CS-4 attachment of the KLY-5 kappabridge in the M^{3}Ore Lab at the University of St. Andrews. The samples were first cooled to −194°C and the susceptibility of the samples was measured until the temperature reached 0°C. The samples were then heated at a rate of 12°C/min in an argon atmosphere from room temperature to 700°C and then cooled back to room temperature. The heated sample was subsequently again cooled to −194°C and the bulk magnetic susceptibility was measured until the sample reached 0°C.

2.1.2. Anisotropy of Magnetic Remanence Analysis

AARM and low-field AIRM were measured on five representative cores or specimens (CB-15C2, CB-19A1, CB-46A1, CB-55A1 and CB-61B2). AARM and AIRM measurements allow the determination of a second rank symmetric tensor from which eigen parameters similar to the AMS tensor parameters (Jelínek, 1977; McCabe et al., 1985). AARM and AIRM measurements were performed at the University of St. Andrews M^{3}Ore Lab. Samples were demagnetized and magnetized with AGICO's LDA5 and PAM1 instruments and magnetic remanence was measured in the JR-6a spinner magnetometer in a near zero field space. The samples were demagnetized using 100 mT alternating field (AF) with an automatic 2-axis tumbling specimen holder prior to imparting an anhysteretic remanence magnetization (ARM) on 15 sample orientations according to the orientation scheme of Hext (1963) and Jelínek (1977). The ARM was imparted using a bias DC field of 50 μT in a peak AF of 100 mT. For AIRM, the samples were imparted with an isothermal remanence magnetization (IRM) in the 15 orientations using a single, one second pulse DC field of 20 mT. The samples were demagnetized in a peak AF of 120 mT before imparting the IRM on each position. In order to test if phases/grains with higher coercivity, such as SD magnetite, have a different fabric compared to the remanence fabric of the full coercivity spectra, we also performed pAARM on the selected cores. To limit the potential effects of switching field angular dependence on pAARM (Finn & Coe, 2020; Nørgaard Madsen, 2004), the pAARM was imparted on 12 sample positions (see the supporitng information for analytical details). The AARM and AIRM data were processed with the REMA6 software (Chadima et al., 2018).

Coe (1966) queries the applicability of describing AIRM using a second rank tensor, taking that study into account we evaluated the calculated AIRM tensor elements and the results of the evaluation are presented in the supporting information (Figure S2).

Stepwise ARM demagnetization and saturation isothermal remanence magnetization (sIRM) measurements were also performed on the samples used for AARM and AIRM analysis (Figure S3). During sIRM acquisition, the samples were first magnetized with the PAM1 in DC fields up to 20 mT and later magnetized with an MMPM10 pulse magnetizer from Magnetic Instruments in DC fields between 25 mT and 3 T.

2.2. Petrofabric Analyses Using X-Ray Computed Microtomography

In order to assess the petrofabric, the same five representative specimens (CB-15C2, CB-19A1, CB-46A1, CB-55A1 and CB-61B2) were imaged by μXCT. The speciemens were scanned with a Nikon Metrology XT H 225 ST X-ray microtomograph at the Natural History Museum, University of Oslo. μXCT analyses was conducted using a 140 kV acceleration voltage, a current of 300 μA, 1 s exposure time and 3,016 rotational projections and using a 0.25 mm copper filter. The X-rays transmitted through the specimen were collected on a planar 1,920 × 1,536 pixels detector. The resulting voxel (volume pixel) size was about 16 μm^3 (see Table S1).

The obtained stack of 1,534 grayscale images on each core represents the attenuation of the X-rays in the scanned volume, that is, phases of higher densities have lighter grayscale voxels and lower density phases have darker voxels. Magnetite and amphibole grains have comparatively higher densities than the groundmass and can therefore easily be distinguished in the scan slices. Plagioclase phenocrysts could not be separated from the scan slices due to similar densities as the sample groundmass. Beam-hardening effects are visible on the scan slices and are most distinct 1.5–2 mm from the edge of the core. Beam-hardening had no effect on magnetite segmentation due to its high attenuation of X-rays, however amphibole segmentation was strongly affected. As a consequence, a 1.5–2 mm rim of the scanned core was segmented as a single blob and removed from the sample set during the manual separation of the data.

Samples were oriented in the scanner to facilitate direct comparison to AMS and anisotropy of magnetic remanence results. However, minor discrepancies in the comparison between AMS and crystal SPO and spatial distribution data collected with μXCT could have been induced by differences in sample mounting.

2.2.1. Extraction of Grain Properties From X-Ray Micro-Computed Tomography Scans

X-ray microtomography scan slices were subsequently analyzed using Blob3D (Ketcham, 2005). Six hundred slices of 1,534 (~40% of the scanned volume) were processed for each specimen in order to limit the segmentation time. For specimen CB-61B2, 1,180 of 1,535 slices were processed to separate magnetite crystals. Blobs of segmented crystals were created from the stacked slices in Blob3D using grayscale threshold values. Noise in the scan slices was limited by removing islands below a certain pixel radius, as well as removing already separated components (only for amphibole segmentation; see Table S1 for Blob3D segmentation parameters). The created blobs were then reviewed, and crystal aggregates were manually separated into individual crystals before data extraction. Crystals smaller than 1,000 voxels for amphibole and 500 voxels for magnetite were discarded to avoid imaging artifacts. Crystals intersected by the edges of the core and processed scan slices were mostly discarded, however, if the shape and length of the intersected blob were not compromised by the intersecting surface they were not discarded. For each crystal grain, the volume, center x, y, z coordinates and the length and orientation of the three orthogonal principal axes (long axis v_1; intermediate axis v_2; short axis v_3) were determined by fitting a best-fit ellipsoid to the separated grain volume surfaces in Blob3D.

We validated the accuracy of the phase separation between Blob3D and the commercial software Avizo Fire edition (Figure S4). In Avizo, magnetite and amphibole were separated from the scanned cores using grayscale thresholding. Magnetite grains smaller than 1,000 to 2,000 voxels and amphibole grains smaller than 3,000 to 4,000 voxels were removed to limit noise and the erosion tool was employed to remove breakdown rims on crystals and imaging artifacts. No individual review of separated crystal volumes was performed in Avizo, which resulted in fast extraction of data, but the crystal volumes extracted largely represent crystal aggregates. The results from Blob3D and Avizo were concordant (see Figure S4): All μXCT data presented below were extracted with Blob3D.

Table 1
Abbreviations and Nomenclature

Magnetic fabrics	AMS	Anisotropy of magnetic susceptibility
	AARM	Anisotropy of anhysteretic remanent magnetization
	AIRM	Anisotropy of isothermal remanent magnetization
Petrofabric	OT	Orientation tensor
	FT	Fabric tensor
	DA	Distribution anisotropy tensor
Ellipsoid axes	x_1	Long axis
	x_2	Intermediate axis
	x_3	Short axis
AMS	k_x	Principal axes of susceptibility of a specimen
	K_x	Mean tensor of susceptibility of a sample
AARM and AIRM	R_x	Principal axes of remanence of a specimen
μXCT	v_x	Individual crystal best-fit ellipsoid axes
	O_x	OT mean best-fit ellipsoid axes
	V_x	FT mean best-fit ellipsoid axes
	λ_x	Distribution anisotropy mean vectors

2.2.2. Crystal Orientation and Fabric Determination

The statistical petrofabric analysis was performed with the TomoFab v. 1.3. MATLAB package by using either a set of grain principal axes directions, or a set of grain principal axes directions and lengths (see details and discussion in Petri et al., 2020). The nomenclature used to describe the magnetic fabrics and the petrofabric is given in Table 1.

First, we calculated the mean principal directions (O_1, O_2, and O_3) by constructing the orientation tensor (OT) for each principal axis group (v_1, v_2 and v_3), as defined by Scheidegger (1965) and Watson (1966) as:

$$OT_{Vi} = \begin{bmatrix} \sum l_{vi,j}^2 & \sum l_{vi,j} m_{vi,j} & \sum l_{vi,j} n_{vi,j} \\ \sum m_{vi,j} l_{vi,j} & \sum m_{vi,j}^2 & \sum m_{vi,j} n_{vi,j} \\ \sum n_{vi,j} l_{vi,j} & \sum n_{vi,j} m_{vi,j} & \sum n_{vi,j}^2 \end{bmatrix}$$

with l, m, n being the directional cosines of either v_1 or v_2 or v_3. The mean v_1, v_2, and v_3 orientations (O_1, O_2 and O_3) were calculated from the OT_{v1}, OT_{v2}, and OT_{v3} maximum eigenvalues and associated eigenvectors. The three resulting mean orientations will likely not be orthogonal, but this approach allows the calculation of well-established criteria for rock fabric estimates: The *K-index* of Woodcock (1977) using OT_{V1} (0 for rotational oblate to 1 for triaxial neutral to ∞ for rotational prolate), and the *LS-index* of Ulrich and Mainprice (2005) using OT_{V1} and OT_{V3} (0 for rotational oblate to 0.55–0.6 for triaxial neutral to 1 for rotational prolate).

Second, we compiled the fabric tensor (FT) that simultaneously integrates the orientation (l, m, n as directional cosines) and length ($\| v_{i,j} \|$) of the three principal axes of best-fit ellipsoids (v_1 and v_2 and v_3), weighted by the individual axis length (i.e., the linear FT of Petri et al., 2020):

$$FT = \sum_{j=1}^{N} \| v_{1,j} \| a_{v1,j} a_{v1,j}^T + \sum_{j=1}^{N} \| v_{2,j} \| a_{v2,j} a_{v2,j}^T + \sum_{j=1}^{N} \| v_{3,j} \| a_{v3,j} a_{v3,j}^T$$

$$\text{with } \sum_{j=1}^{N} \| v_{1,j} \| a_{v1,j} a_{v1,j}^T = \begin{bmatrix} \sum \| v_{1,j} \| l_{v1,j}{}^2 & \sum \| v_{1,j} \| l_{v1,j} m_{v1,j} & \sum \| v_{1,j} \| l_{v1,j} n_{v1,j} \\ \sum \| v_{1,j} \| m_{v1,j} l_{v1,j} & \sum \| v_{1,j} \| m_{v1,j}{}^2 & \sum \| v_{1,j} \| m_{v1,j} n_{v1,j} \\ \sum \| v_{1,j} \| n_{v1,j} l_{v1,j} & \sum \| v_{1,j} \| n_{v1,j} m_{v1,j} & \sum \| v_{1,j} \| n_{v1,j}{}^2 \end{bmatrix}$$

The eigenvalues and eigenvectors of the FT correspond to the three mean axes ($V_1 \geq V_2 \geq V_3$). The shape of the FT ellipsoid can then be projected in Ramsay-type diagrams by calculating the V_1/V_2 and V_2/V_3 mean axes length ratios, but also by calculating the corrected degree of anisotropy (P') and the shape parameter (T) as done with the AMS tensor elements (see above and Petri et al., 2020). The FT approach described here also allows one to calculate 95% confidence estimates around the mean principal axes using the method of Jelínek and Kropáček (1978). The results of the two approaches are presented in Table 2.

2.2.3. Distribution Anisotropy Analysis

We evaluated the spatial distribution of grains, that is, DA, by calculating directional cosines l, m, n of the vector defined by two grain centers, for each couple of grains in the sample segmented using Blob3D. The sets of directional cosines, were then used to compile a distribution anisotropy tensor, similar to an OT, and defined as:

$$DA = \begin{bmatrix} \sum w l_j^2 & \sum w l_j m_j & \sum w l_j n_j \\ \sum w m_j l_j & \sum w m_j^2 & \sum w m_j n_j \\ \sum w n_j l_j & \sum w n_j m_j & \sum w n_j^2 \end{bmatrix}$$

Each vector of the directional cosines is here weighted by the w-factor of Stephenson (1994), defined as:

$$w = \frac{\omega_1 + \omega_2}{\pi r^3}$$

with ω_1 and ω_2 being the volumes of the two grains, and r the distance between the same two grains. The use of the weighting factor implies that large grains that are spatially close together have a stronger influence on the result compared to small and distant grains. This also avoids the calculated DA to be affected by the shape of the sample (two grains at each side of an elongated sample are unlikely to impact the DA). The spatial distribution of grains is deduced from the corrected degree of anisotropy (P') and the shape (T) of the ellipsoid defined by the eigenvectors and associated eigenvalues of the DA ($\lambda_1 \geq \lambda_2 \geq \lambda_3$): Low degree of anisotropy (low P') indicates that grains are randomly distributed; high degree of anisotropy (high P') indicates that grains are strictly distributed, either in planes if the shape of the DA is oblate ($T > 0$) or along lines if the shape of the DA is prolate ($T < 0$). The orientation of the planes or lines onto which grains are distributed are determined by the DA eigenvectors, λ_1 being the line, and λ_3 the pole to the plane. This method is implemented in the Tomofab MATLAB code (version 1.3). We analyzed the DA of the complete data set but also as three equivalent subsets of grains based on their volume.

3. Magnetic Properties and Magnetic Fabrics

3.1. Magnetic Properties

At room temperature, the bulk magnetic susceptibility of samples CB-15, CB-19, CB-46, CB-55 and CB-61 ranges from 16.6×10^{-3} to 4.2×10^{-3} SI (Table 2). The bulk magnetic susceptibility is homogeneous between the different specimens of each sample.

At sub-zero temperatures, thermomagnetic susceptibility (T-X) curves of samples CB-19 and CB-46 show an increase in bulk magnetic susceptibility between −180 to −160°C before the susceptibility slowly decreases until −50°C, this represents the Verwey transition (Figures 2l and 2m). A Verwey transition feature is not observed in samples CB-15, 55 and 61, instead susceptibility steadily decrease from −194°C to −120°C before steadily increasing toward 0°C (Figures 2k, 2n and 2o). During heating from 25°C to 400°C, all samples show an inflection at around 300°C. Samples CB-15, 55 and 61, that do not display a Verwey transition, exhibit the most abrupt increase in susceptibility (50%–75%), whereas CB-19 and CB-46 exhibit relatively modest increase in susceptibility (20%–40%). Heating from 400 to 700°C reveals a prominent decrease in susceptibility in all samples between 450°C and 580°C; samples CB-19 and 46 peak between 550°C to 580°C, while samples CB15, 55 and 61 exhibit broader peaks ranging from 450°C to 550°C. For all, irreversible cooling curves are produced, and the 300°C inflection recorded during heating is absent. Samples

Table 2
AMS, AARM and Tomofab Fabric, Orientation, Distribution Anisotropy Tensors and Fabric Parameters

AMS		K_m				K_1d	K_1i	$K_1\sigma$	K_2d	K_2i	$K_2\sigma$	K_3d	K_3i	$K_3\sigma$
Sample	N	10^{-3} SI (std. err.)	T	P	P'	(deg)	(deg)	(max/min)	(deg)	(deg)	(max/min)	(deg)	(deg)	(max/min)
CB-15C2		16.28	−0.367	1.069	1.07	102	42	2/1	195	3	4/2	289	48	4/1
CB-15	**5**	**16.6 (0.3)**	**−0.387**	**1.068**	**1.07**	**104**	**37**	**4/1**	**197**	**4**	**3/1**	**292**	**52**	**4/2**
CB-19A1		4.14	−0.421	1.012	1.012	11	42	1/1	224	43	3/1	117	17	3/1
CB-19	**5**	**4.24 (0.31)**	**−0.498**	**1.013**	**1.014**	**13**	**37**	**6/3**	**204**	**52**	**12/6**	**107**	**5**	**12/3**
CB-46A1		9.65	0.522	1.018	1.018	10	16	1/3	146	68	0/1	276	15	0/0
CB-46	**6**	**9.35 (0.57)**	**0.287**	**1.019**	**1.019**	**23**	**12**	**9/6**	**142**	**67**	**9/1**	**289**	**20**	**8/3**
CB-55A1		15.13	0.892	1.07	1.079	317	61	2/0	150	28	2/0	57	6	0/0
CB-55	**11**	**15.25 (0.55)**	**0.899**	**1.066**	**1.074**	**158**	**52**	**52/3**	**323**	**38**	**52/2**	**59**	**7**	**3/2**
CB-61B2		11.65	0.785	1.046	1.051	185	38	18/2	63	34	2/18	307	34	2/2
CB-61	**6**	**11.53 (0.46)**	**0.854**	**1.045**	**1.05**	**185**	**40**	**16/4**	**58**	**36**	**16/2**	**304**	**30**	**5/2**
AARM		R_m				R_1d	R_1i	$R_1\sigma$	R_2d	R_2i	$R_2\sigma$	R_3d	R_3i	$R_3\sigma$
Sample		(10^{-3} A/m)	T	P	P'	(deg)	(deg)	(E12/E13)[a]	(deg)	(deg)	(E23/E21)	(deg)	(deg)	(E32/E31)
CB-15C2		46.02	−0.417	1.418	1.432	104	39	61/53	196	2	79/61	288	51	79/53
CB-19A1		9.747	−0.573	1.093	1.099	24	45	89/89	166	38	90/89	273	20	90/89
CB-46A1		21.1	0.455	1.232	1.240	20	22	90/88	141	52	89/90	277	30	89/88
CB-55A1		36.91	0.937	1.312	1.362	323	25	90/81	161	64	82/90	57	7	82/81
CB-61B2		31.47	0.751	1.219	1.241	192	34	82/45	69	38	49/82	308	33	49/45
AIRM		R_m				R_1d	R_1i	$R_1\sigma$	R_2d	R_2i	$R_2\sigma$	R_3d	R_3i	$R_3\sigma$
Sample		(10^{-3} A/m)	T	P	P'	(deg)	(deg)	(E12/E13)	(deg)	(deg)	(E23/E21)	(deg)	(deg)	(E32/E31)
CB-15C2		3.466	−0.273	1.479	1.486	101	42	20/14	196	5	38/20	291	47	38/14
CB-19A1		0.535	0.277	1.07	1.071	37	20	41/18	251	66	27/41	131	13	27/18
CB-46A1		1.286	0.145	1.131	1.132	8	35	23/11	158	52	19/23	267	15	19/11
CB-55A1		3.095	0.926	1.437	1.508	206	82	62/5	324	4	5/62	54	8	5/5
CB-61B2		2.237	0.733	1.278	1.306	163	49	47/9	52	18	11/47	308	36	11/9
Tomofab-FT						V_1d	V_1i	$V_1\sigma$	V_2d	V_2i	$V_2\sigma$	V_3d	V_3i	$V_3\sigma$
Sample	Phase	N	*K-index*	*LS*	T	P'	(deg)	(deg)	(E12/E13)	(deg)	(deg)	(E23/E21)	(deg)	(deg)	(E32/E31)
CB-15C2	Amp	2,635	3.889	0.801	−0.678	1.662	91	40	3/1	188	9	16/3	288	49	16/1
	Mgt	2,289	0.284	0.194	0.539	1.076	105	47	52/16	268	42	11/52	6	8	12/17
CB-19A1	Amp	8,336	0.752	0.347	0.077	1.376	175	48	4/1	268	3	4/4	1	42	4/1
	Mgt	3,577	0.134	0.117	0.747	1.079	121	48	61/12	278	40	9/61	18	11	10/13
CB-46A1	Amp	5,170	0.408	0.233	0.415	1.404	4	22	6/2	237	56	3/6	104	24	4/2
	Mgt	2,470	0.071	0.074	0.959	1.09	202	10	84/13	299	34	13/84	98	55	12/16
CB-55A1	Amp	3,699	0.055	0.044	0.847	1.596	343	72	15/2	134	16	2/15	226	8	3/2
	Mgt	2,869	0.048	0.082	0.793	1.099	319	7	63/7	85	78	14/63	228	10	14/6
CB-61B2	Amp	4,126	0.406	0.49	0.308	1.517	134	45	6/1	249	24	3/5	358	36	3/2
	Mgt	3,907	0.243	0.229	0.561	1.064	129	55	45/13	337	32	15/45	238	14	17/12

Table 2
Continued

Tomofab-OT	Phase	*N*	*K-index*	*LS*	*T*	*P′*	O_1d (deg)	O_1i (deg)	O_2d (deg)	O_2i (deg)	O_3d (deg)	O_3i (deg)	
CB-15C2	Amp	2,635	3.889	0.801			91	41	253	49	346	20	
	Mgt	2,289	0.284	0.194			108	53	275	25	6	8	
CB-19A1	Amp	8,336	0.752	0.347			174	47	283	25	10	32	
	Mgt	3,577	0.134	0.117			135	67	292	4	19	11	
CB-46A1	Amp	5,170	0.408	0.233			5	20	264	30	103	39	
	Mgt	2,470	0.071	0.074			222	20	318	33	100	54	
CB-55A1	Amp	3,699	0.055	0.044			345	73	141	6	227	8	
	Mgt	2,869	0.048	0.082			320	11	329	50	228	9	
CB-61B2	Amp	4,126	0.406	0.49			134	46	345	34	10	32	
	Mgt	3,907	0.243	0.229			128	52	355	64	237	15	
Tomofab-DA	Phase	*N*	*K-index*	*LS*	*T*	*P′*	λ_1d (deg)	λ_1i (deg)	λ_2d (deg)	λ_2i (deg)	λ_3d (deg)	λ_3i (deg)	Nearest neighbor (mm)
CB-15C2	Amp	2,635	0.833		0.091	1.179	269	41	124	43	16	19	–
	Mgt	2,289	0.782		0.122	1.254	89	38	191	14	297	49	0.48 (sd. 0.37)
CB-19A1	Amp	8,336	0.171		0.708	1.173	291	51	101	39	195	5	–
	Mgt	3,577	1.017		−0.008	1.205	187	44	85	12	344	44	0.42 (s.d. 0.29)
CB-46A1	Amp	5,170	1.624		−0.238	1.12	288	24	18	1	112	66	–
	Mgt	2,470	0.074		0.862	1.294	204	58	14	31	106	5	0.53 (s.d. 0.35)
CB-55A1	Amp	3,699	1.223		−0.102	1.074	299	60	109	30	201	4	–
	Mgt	2,869	0.367		0.462	1.262	317	56	126	33	220	5	0.45 (s.d. 0.34)
CB-61B2	Amp	4,126	0.393		0.437	1.151	341	27	103	46	233	32	–
	Mgt	3,907	0.368		0.462	1.227	130	36	244	29	2	41	0.45 (s.d. 0.38)

Abbreviations: AARM, anisotropy of anhysteretic remanent magnetization; AIRM, anisotropy of isothermal remanent magnetization; AMS, anisotropy of magnetic susceptibility.
[a]The errors associated with the tensor calculation is much smaller when using the 12-position measurement scheme. See Table S2.

CB-15 and CB-55 show a ∼20% decrease in magnetic susceptibility after cooling, CB-61 exhibits a modest 5%–10% increase and samples CB-46 and CB-19 display a marked increase in susceptibility of 40% and 500% respectively (Figures 2k–2o).

The observation of a Verwey transition at around −170°C and/or Curie temperatures between 540°C and 580°C show that a low titanium titanomagnetite is the main ferrimagnetic phase in the samples (Dunlop & Özdemir, 1997; Lattard et al., 2006). The irreversible inflection at around 300°C on all heating curves indicates that the magnetic mineralogy changed during the experiment. In CB-15, CB-46 and CB-55, a relatively modest change of <20% is recorded and this may be attributed to the combined effect of titanium exsolution from titanomagnetite and the modification of maghemite during the high temperature experiment (Bilardello, 2020; Dunlop & Özdemir, 1997; Özdemir et al., 1993). Abrupt increases in susceptibility in CB-46 and especially in CB-19 show that a substantial amount of new magnetite has formed during the experiment. For simplicity, we will refer to low Ti-magnetite as magnetite in subsequent paragraphs.

The ARM AF demagnetization of the samples shows M/Mmax = 0.9 (i.e., when 90% of the imparted field is gone) at around an AF of 50 mT for CB-15, 55 and 61 and around an AF of 70 mT for CB-19 and 46 (Figure S3). The sIRM acquisition curves show that CB-19 and 46 reach 95% saturation in fields ≥400 mT (Figure S3). Sample CB-19 has the highest coercivity range of all of the samples studied and the thermomagnetic susceptibility experiment shows that this sample also has a very prominent Hopkinson peak (Figure 2l).

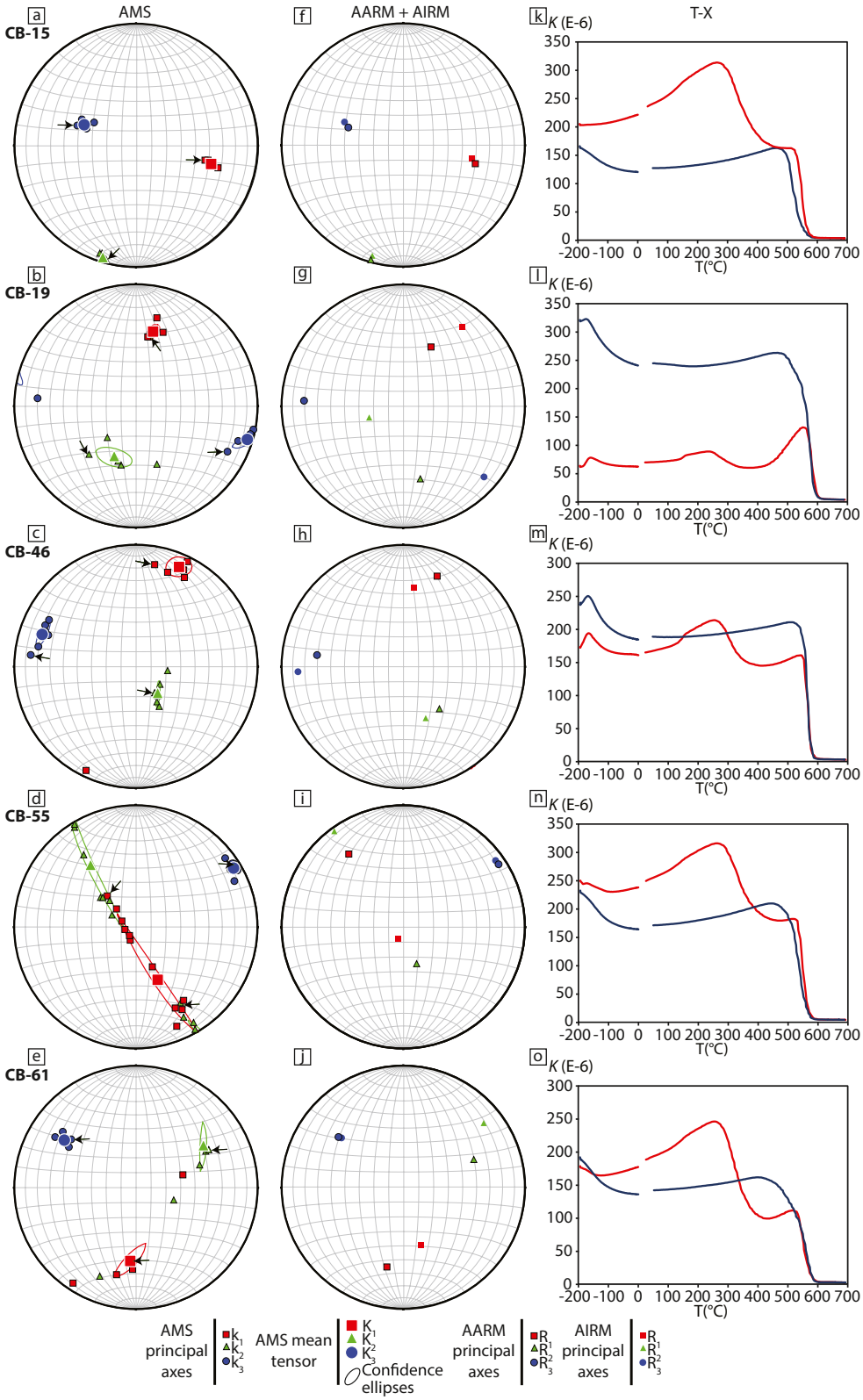
a
CB-15
AMS
f
AARM + AIRM
k
T-X
K (E-6)
T(°C)
b
CB-19
g
l
c
CB-46
h
m
d
CB-55
i
n
e
CB-61
j
o
AMS principal axes
AMS mean tensor
Confidence ellipses
AARM principal axes
AIRM principal axes

Together these data indicate that single domain or pseudosingle domain magnetite is present and may play a dominant role in the magnetic fabric in this sample (cf. Dunlop & Özdemir, 1997). Sample CB-46 returns a similarly high coercivity spectra and also exhibits a prominent Verwey transition and notable Hopkinson peak on the thermomagnetic susceptibility curve (Figures 2m and S3). In contrast, CB-15, 55 and 61 reach 95% saturation at an applied field of ∼300 mT (Figure S3), and exhibit a more gradual Curie temperature peak and record no Verwey transition (Figures 2k, 2n and 2o). This points toward the dominance of a relatively low-coercivity ferrimagnetic phase in these samples. The absence of a Verwey transition indicates the presence of non-stoichiometric likely oxidized magnetite and/or superparamagnetic (SP) magnetite grains in these samples (Moskowitz et al., 1989; Özdemir et al., 1993).

3.2. Magnetic Fabrics

While AMS parameters in the Cerro Bayo intrusion show significant variation between samples ($P' = 1.008$ to 1.081 and $T = -0.799$ to 0.974; Burchardt et al., 2019), sub-samples or specimens collected from each sample return highly consistent results. The samples selected for detailed petrofabric μXCT analysis were purposefully chosen from a range of samples to include a broad selection of AMS fabric types.

3.2.1. CB-15

The mean AMS ellipsoid for CB-15 AMS has a $P' = 1.07$ (ranging from 1.068 to 1.073) and a $T = -0.39$ (ranging from −0.442 to −0.361), this defines a moderately prolate fabric. Sub-sample AMS axes define very narrow confidence ellipses (Figure 2 and Table 2). Both the AARM and AIRM principal axes are coaxial to the AMS axes, but have higher P' values (Figure 2 and Table 2).

3.2.2. CB-19

The mean AMS ellipsoid for CB-19 has a $P' = 1.01$ (ranging from 1.012 to 1.015) and a $T = -0.5$ (ranging from −0.675 to −0.309), this defines a very weak, moderately prolate fabric. The k_1 axes are clustered and k_2 and k_3 axes define a broad girdle (Figure 2 and Table 2). The principal axes of the AMS, AARM and AIRM ellipsoids are slightly oblique and diverge by 15–30°. The pAARM R_3 axes of CB-19A1 are coaxial to the 12-position calculated AARM principal axes, but not the 15-position calculated principal axes (Figures 2, S5 and Table S2).

3.2.3. CB-46

The mean AMS ellipsoid for CB-46 AMS has a $P' = 1.02$ (ranging from 1.018 to 1.023) and a $T = 0.29$ (ranging from 0.522 to 0.131), this defines a weakly anisotropic, transitional oblate fabric. Sub-sample AMS axes are tightly clustered (Figure 2 and Table 2). The principal axes of the AMS, AARM, AIRM and pAARM ellipsoids plot close to each other (Figure S5 and Table S2).

3.2.4. CB-55

The mean AMS ellipsoid for CB-55 has a $P' = 1.07$ (ranging from 1.064 to 1.087) and a $T = 0.9$ (ranging from 0.91 to 0.599), k_3 axes are tightly clustered; k_1 and k_2 axes plot along a girdle defining an oblate ellipsoid (Figure 2 and Table 2). The maximum and intermediate axes of the AMS, AARM and AIRM ellipsoids plot along the same girdle, whereas the minimum axes of the AMS, AARM and AIRM are coaxial. The R_3 axes of the pAARM and AARM are nearly coaxial (Figure S5 and Table S2).

Figure 2. Anisotropy of magnetic susceptibility (AMS) specimen principal axes (k) and sample mean tensor (K) (a–e) of the cores from sample CB-15, CB-19, CB-46, CB-55 and CB-61 plotted in equal-area lower-hemisphere Schmidt-nets. Black arrows indicate the AMS principal axes of CB-15C2, CB-19A1, CB-46A1, CB-55A1 and CB-61B2. Confidence ellipses (95%) were calculated with Jelínek statistics. (f–j) Anisotropy of anhysteretic remanence magnetization (AARM) and anisotropy of isothermal remanence magnetization (AIRM) principal axes of CB-15C2, CB-19A1, CB-46A1, CB-55A1 and CB-61B2. (k–o) Temperature versus susceptibility curves for samples CB-15, CB-19, CB-46, CB-55 and CB-61. See text for details.

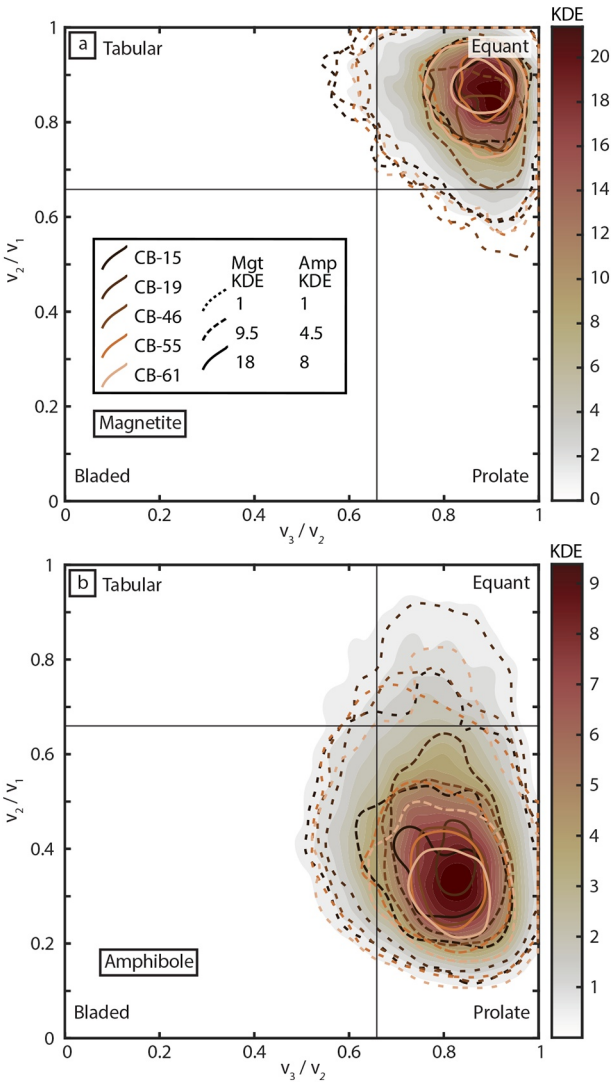

Figure 3. Zingg diagram with kernel density estimate (KDE) contours of (a) magnetite crystal axial ratios and (b) amphibole compiled from all specimens. The lines represent KDE levels for CB-15C2, CB-19A1, CB-46A1, CB-55A1, CB-61B2.

3.2.5. CB-61

The mean AMS ellipsoid for CB-61 has a mean $P' = 1.05$ (ranging from 1.046 to 1.055) and a $T = 0.85$ (ranging from 0.639 to 0.974). k_1 and k_2 sub-sample axes define a girdle and k_3 axes are clustered, these data describe a strongly oblate fabric (Figure 2 and Table 2). The AMS, AARM and AIRM maximum and intermediate axes plot along a single girdle and the corresponding minimum axes are coaxial to one another. The pAARM R_3 principal axis are nearly coaxial to the AARM R_3 (Figure S5 and Table S2).

4. Petrofabric

4.1. Grain Shape

In total, 15,112 magnetite and 23,966 amphibole grains were separated from the five representative scanned cores (see details in Table 2). Magnetite and amphibole both occur as individual "free-floating" grains in the groundmass and as aggregates (Figures 1a–1f). Even though the whole core was not processed with Blob3D, the limited treated volume still yields >2,000 separated crystals per mineral phase and specimen, which is adequate for crystal population statistics (cf. Mock & Jerram, 2005; Morgan & Jerram, 2006). In all five specimens magnetite grains have similar crystal habits (Figure 3). Separated single magnetite grains are equant, display a nearly cubic crystal habit and have an average v_1/v_3 axis ratio (aspect ratio) of 1.44 (0.24 s.d.) and v_1/v_2 axis ratio of 1.21 (0.15 s.d.) ($n = 14{,}828$) (Figure 3a). Visual inspection of magnetite crystals with a scanning electron microscope show that magnetite clusters consist of both individual crystals with distinct margins and intergrown crystals (Figures 1b and 1c). The v_1 lengths of extracted crystals range from 0.15 to 0.9 mm and the bulk (~80%) of the total analyzed volume of magnetite in the samples is carried by grains with v_1 lengths of between 0.18 and 0.5 mm (Figures 4a and 4b). Crystals that were intersected by the edge of the core and scans were excluded from the crystal size distribution and crystal shape analyses. The average distance between magnetite crystal centers to its nearest neighbor ranges from 0.53 to 0.42 mm (Table 2; Mattsson et al., 2021). About 50%–60% of the magnetite crystals in the analyzed samples have a d/r ratio >0.5 and between 40% to 50% of the crystals have a ratio >0.8 to its nearest neighbor (see Introduction for description of ratio).

The amphibole grains in all specimens are dominantly prolate with an average v_1/v_3 axis ratio of 3.49 and v_1/v_2 axis ratio of 2.71 ($n = 22{,}243$) (Figures. 1a, 1b, 1e, 1f and 3b). The v_1 lengths of amphiboles extracted from the scanned cores range between 0.2 to 5.4 mm (Figure 4c).

4.2. Crystal Shape Preferred Orientations

4.2.1. CB-15

The magnetite long axis (v_1) orientations present a moderately defined E-W striking girdle (Figure 5a). Conversely, the magnetite short axis (v_3) orientations are characterized by a horizontal N-striking cluster. The analysis of the FT shows that V_1 is located at 105 / 47 and V_3 at 006 / 08, both are coaxial with the OT (Figure 5a and Table 2). The fabric parameters derived from the FT indicate a moderately defined oblate fabric ($T = 0.54$, $P' = 1.08$), which is consistent for all crystal sizes (Figure 6a; Table S3). The constrained FT-foliation is oriented 186 / 82 (dip-direction).

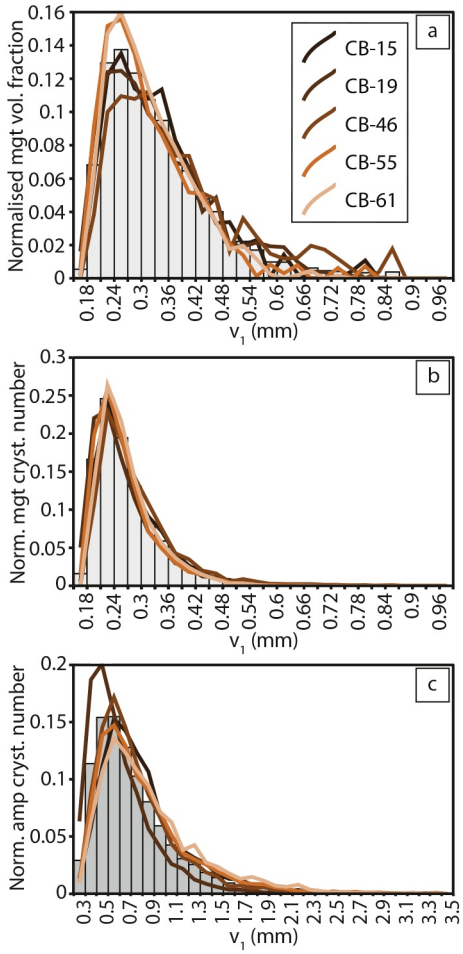

Figure 4. (a) Fraction of grains of the total magnetite volume and (b) normalized number of magnetite crystals versus crystal long axis length in samples CB-15C2, CB-19A1, CB-46A1, CB-55A1 and CB-61B2. Magnetite crystals are sorted into 0.03 mm-sized bins based on long-axis length. The volume/number of magnetite in a bin was normalized by the total volume/number of extracted magnetite grains from the specimen. The lines in the plot represent the individual specimens and the histogram bars in the background are compiled from all extracted crystals. About 80% of all magnetite in the specimens is carried by crystals with v_1 lengths between 0.18 and 0.5 mm. (c) Number of amphibole crystal versus crystal v_1 length in specimen CB-15C2, CB-19A1, CB-46A1, CB-55A1 and CB-61B2. Amphibole crystals are sorted into 0.1 mm-sized bins. Crystals that were intersected by the edge of the core and scans were excluded from the crystal size distribution analyses.

In contrast to magnetite, amphibole grains document a fabric that is more clearly defined (Figure 5b). v_1 orientations present a distinct cluster to the east. Conversely, v_3 orientations plot along a weak N-S striking girdle that dips moderately to the west. The FT governed by the amphibole v_1, results in a V_1 at 091 / 40, which is oriented very close to the O_1, whereas the V_3 plots on the v_3 girdle at 288 / 49, far from the O_3. The fabric parameters obtained by the FT analysis indicate a strongly anisotropic, prolate fabric ($P' = 1.66$; $T = -0.68$), with a weakly constrained foliation at 108 / 41 (dip-direction).

4.2.2. CB-19

The v_1 of magnetite grains are aligned along a steeply dipping E-W girdle and v_3 axes cluster at the poles of the Schmidt net (Figure 5c). The V_1 at 121 / 48 is not aligned with respect to O_1 but still located on the v_1-defined girdle (Figure 5c and Table 2). The V_3 axis at 018 / 11 is almost identical to the O_3. The FT fabric parameters indicate an oblate ($T = 0.75$) and moderately anisotropic fabric ($P' = 1.08$) with a defined foliation at 198 / 79 (dip-direction).

The amphibole v_1 axes define a weakly developed, moderately southward dipping girdle; v_3 axes define a northward dipping wide cluster (Figure 5d). The V_1 and V_3 are oriented at 175 / 48 and 001 / 42, respectively (Table 2). A triaxial neutral fabric is indicated by the FT fabric parameters ($T = 0.08$) with a strong degree of anisotropy ($P' = 1.38$). The foliation defined by the FT of amphibole lies at 181 / 48 (dip-direction).

4.2.3. CB-46

The v_1 of magnetite grains are aligned along a N-S striking girdle that dips moderately to the west and the v_3 axes cluster to the east (Figure 5e). The V_3 axis constrained by the FT at 098 / 55 correlates well with O_3, whereas the V_1 at 202 / 10 is slightly misoriented with respect to O_1 (Table 2). The analysis of the FT fabric parameters shows a strongly oblate ($T = 0.96$) and moderately anisotropic fabric ($P' = 1.09$); the defined foliation stands at 278 / 35 (dip-direction).

The amphibole v_1 axes plot in a moderately developed, sub-vertical NNE-striking girdle with a cluster around the poles of the Schmidt net; v_3 orientations define a sub-horizontal cluster (Figure 5f). The mean V_1 and V_3 are coaxial to the OT and oriented at 004 / 22 and 104 / 24, respectively (Table 2). The fabric is oblate ($T = 0.42$) with a strong degree of anisotropy ($P' = 1.4$). The foliation defined by the FT of amphibole lies at 284 / 66 (dip-direction).

4.2.4. CB-55

The fabric of CB-55 is very well developed for both magnetite and amphiboles. Magnetite grains v_1 define a clear vertical NW-SE-striking girdle, whereas v_3 orientations occur in a narrow sub-horizontal cluster (Figure 5g). Both orientations and fabric parameters obtained with OT analysis corroborates with the FT analysis (Table 2). The V_1 axis is oriented 319 / 07; V_3 axis lies at 228 / 10; and the fabric is strongly oblate and moderately defined ($T = 0.79$, $P' = 1.1$). The compiled foliation defined by the V_1-V_2 plane lies at 048 / 80 (dip-direction).

Similarly, amphibole v_1 axes define a vertical, NW-SE-striking girdle and a narrow v_3 cluster (Figure 5h). The FT constructed using the amphibole individual axes and length is coaxial to the OT and points to a V_1 at 343 / 72 and V_3 at 226 / 08 with a strongly developed oblate fabric ($P' = 1.6$; $T = 0.85$), and a well-defined foliation of 046 / 82 (dip-direction).

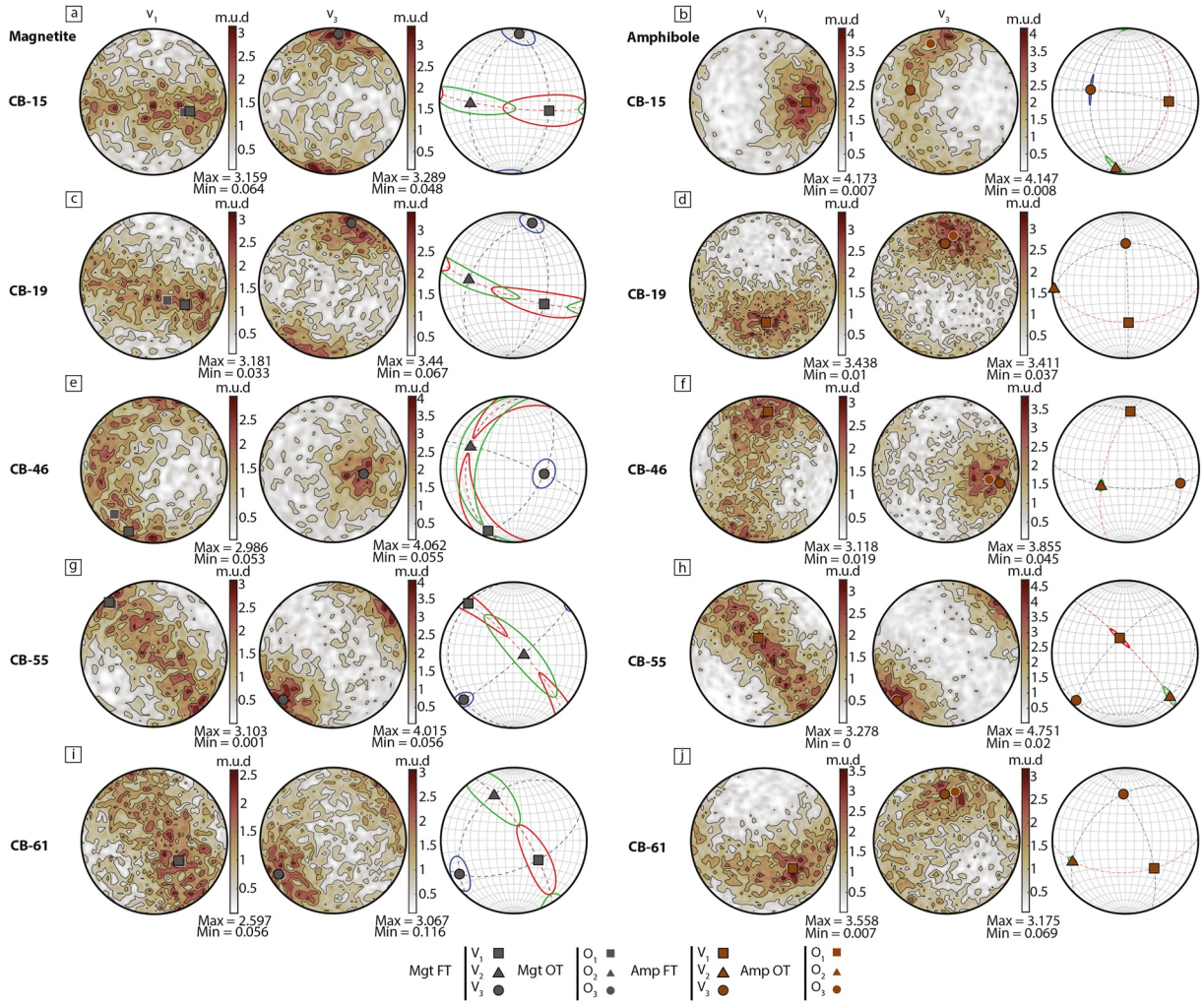

Figure 5. Lower-hemisphere equal-area Schmidt nets showing v_1 and v_3 orientations and the fabric and orientation tensors for magnetite and amphibole populations for sample CB-15C2, CB-19A1, CB-46A1, CB-55A1 and CB-61B2. The v_1 and v_3 axes are represented with multiples of uniform distribution (M.U.D.) contour plots. The mean fabric tensors with confidence ellipses of the tensor analyses created with Tomofab are plotted in lower-hemisphere equal-area Schmidt nets. Confidence ellipses (95%) were calculated with Jelínek statistics.

4.2.5. CB-61

In CB-61, magnetite grains v_1 are distributed in a weakly defined vertical NW-SE-striking girdle, whereas v_3 orientations plot in a sub-horizontal cluster in the SW (Figure 5i). Both orientations and fabric parameters obtained by OT analysis corroborate results with the FT analysis (Table 2). The V_1 axis is oriented 129 / 55; V_3 axis trend and plunge 238 / 14; and the fabric is oblate ($T = 0.56$), but with a relatively low degree of anisotropy ($P' = 1.06$). The foliation defined by the V_1-V_2 plane is oriented 129 / 55 (dip-direction).

Amphibole v_1 in CB-61 has a weak moderately southward dipping girdle distribution. The FT calculation indicates a strong ($P' = 1.52$) transitional oblate fabric ($T = 0.31$) with V_3 at 358/36 and a defined foliation of 178/54 (dip-direction) (Figure 5j and Table 2).

4.3. Distribution Anisotropy of Magnetite

Here we report the results of the DA of magnetite; results for the DA of amphiboles can be found in the supporting information.

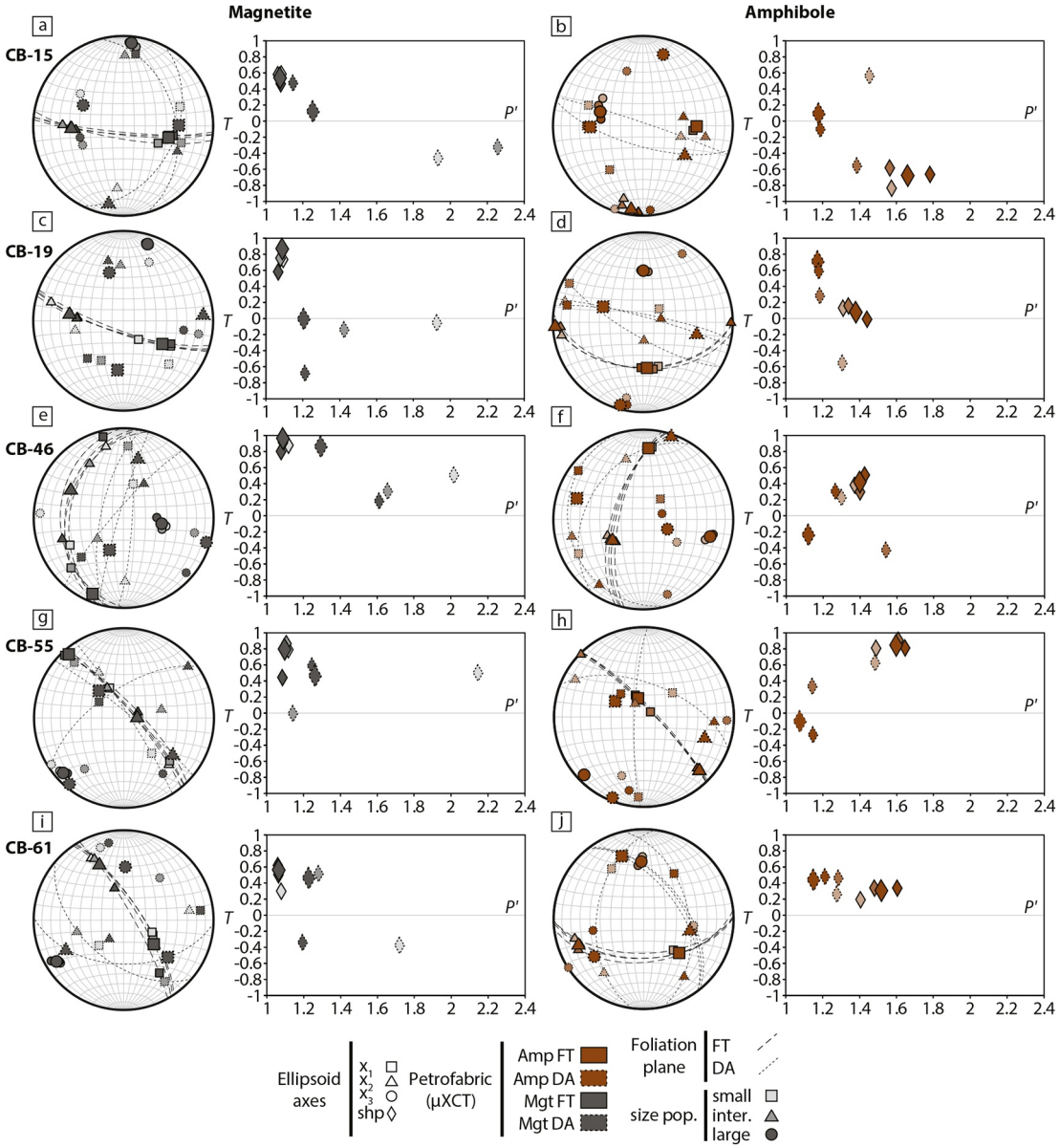

Figure 6. Comparison between fabric tensors (V_x) and distribution anisotropy (λ_x) tensors for different crystal populations of the selected cores. The crystals were sorted based on their volume and separated into three bins of equal number of crystals. A foliation plane was fitted to the V_1-V_2 and λ_1-λ_2 planes if $T > 0$.

4.3.1. CB-15

The magnetite grains of CB-15 are distributed on a NE-SW girdle ($P' = 1.25$, $T = 0.12$; Figure 6a). The DA λ_1 axes (089 / 38) plots close to the V_1 FT axes and together with λ_2 define a foliation oriented 117 / 41 (dip-direction) (Table 2). The analysis of the different grain size categories shows that the magnetite DA is strongly anisotropic for small and intermediate grain sizes, but both the orientation and shape of the DA vary (Figure 6a).

4.3.2. CB-19

The magnetite grains of CB-19 have a triaxial and moderately defined distribution, as indicated by the fabric parameters of the DA ($P' = 1.21$, $T = -0.01$; Figure 6c). The λ_1 and λ_2 eigenvectors are distributed on a southward dipping girdle and define a foliation plane oriented 187 / 44 (dip-direction) that is sub-parallel to the magnetite FT foliation. The analysis of the different grain size categories shows that the small grain

sizes have a relatively strong and transitional prolate distribution coinciding with the southward-dipping girdle. Large and intermediate volume grains define a prolate and transitional prolate fabric with a lineation plunging moderately to the SW (Figure 6c; Table S3).

4.3.3. CB-46

The degree of anisotropy and shape of the DA ($P' = 1.29$ and $T = 0.86$) indicates that magnetite grains are distributed along planar structures (Figure 6e). The orientation of these planes can be assessed by the DA eigenvectors, with λ_1 being 204 / 58 and λ_3 at 106 / 05. The compiled planar structure along which grains are aligned are defined by a plane oriented 286 / 86 (dip-direction). The DA of the different grains size categories display transitional oblate shapes with a high degree of anisotropy (Table S3). However, all the DA foliations are oriented at a high angle to the mean FT axes (Figure 6e).

4.3.4. CB-55

The DA of magnetite grains in CB-55 (Figure 6g) shows an oblate distribution ($T = 0.46$) that is moderately anisotropic ($P' = 1.26$). Magnetite grains are distributed along planes, where the pole to these planes λ_3 (220 / 05) lies close to V_3. Although λ_1 (317 / 56) is highly misoriented with respect to V_1, the compiled foliation defined by the grain spatial distribution (040 / 85, dip-direction) is very close to the foliation defined by the shape and the orientation of the grains (i.e., the FT). These characteristics are consistent for all grain size categories except for intermediate volume magnetite crystals that have a triaxial distribution (Figure 6g).

4.3.5. CB-61

The DA of magnetite grains in CB-61 (Figure 6i) is oblate ($T = 0.46$), with a moderate degree of anisotropy ($P' = 1.23$). Magnetite grains are distributed along moderately S-dipping planes, where the pole to these planes (λ_3 at 002 / 41) coincides with magnetite V_2. λ_1 (130 / 36) plots close to V_1 and the compiled foliation defined by the grain spatial distribution (182 / 49, dip-direction) is almost at a right angle to the FT foliation. The fabric shape and orientation vary between different grain sizes. The smallest and largest volume grains have a prolate distribution and the intermediate volume grains have an oblate distribution (Figure 6i).

5. Interpretation and Discussion

Based on our results, the AMS fabric of the Cerro Bayo trachyandesite may be attributed to three sources: (a) The SPO of magnetite grains (Ferré, 2002; Hrouda, 1982); (b) the spatial distribution of the magnetite grains across the sample (Cañón-Tapia, 1996, 2001; Gaillot et al., 2006; Hargraves et al., 1991; Stephenson, 1994; Grégoire et al., 1995); and (c) the amphibole CPO and composition (Biedermann et al., 2015, 2018). The analysis of these three components of the petrofabric shows contrasting relationships in our samples.

5.1. Comparison Between Magnetic Fabrics and Rock Fabrics

The AMS k_1 and AARM R_1 principal axis in CB-15 are coaxial with the V_1 and O_1 of both magnetite and amphibole (Figure 7a). The magnetite and amphibole SPO are coaxial in terms of maximum principal direction, but not the intermediate direction. The shape parameters that can be derived from the AMS, AARM, amphibole FT, and OT-derived indexes indicate a moderate to strong prolate fabric. The magnetite DA has a triaxial shape and is co-axial to amphibole FT and AMS, AARM and AIRM principal axes, but not the magnetite FT (Figure 7a). The magnetite DA and the amphibole SPO therefore likely control the principal directions of the AMS ellipsoid. The non-coaxial oblate magnetite components of the petrofabric may destructively interfere, which induce prolate magnetic fabrics controlled by the amphibole SPO and/or the intersection lineation between the magnetite components of the petrofabric.

In CB-19, the magnetite FT displays an oblate fabric and the amphibole FT a triaxial fabric with a similar east-west strike of the foliation planes, although the inclination of the amphibole FT foliation is distinctly shallower (Figures 5c, 5d, 6c and 6d). Magnetite DA is triaxial and plots close to the amphibole FT. The AMS and AARM fabrics of CB-19 are prolate and k_1 and R_1 plunge toward the north, whereas amphibole V_1 and magnetite λ_1 plunge toward the south. Amphibole V_3 and magnetite λ_3, in turn correlate with k_1 and

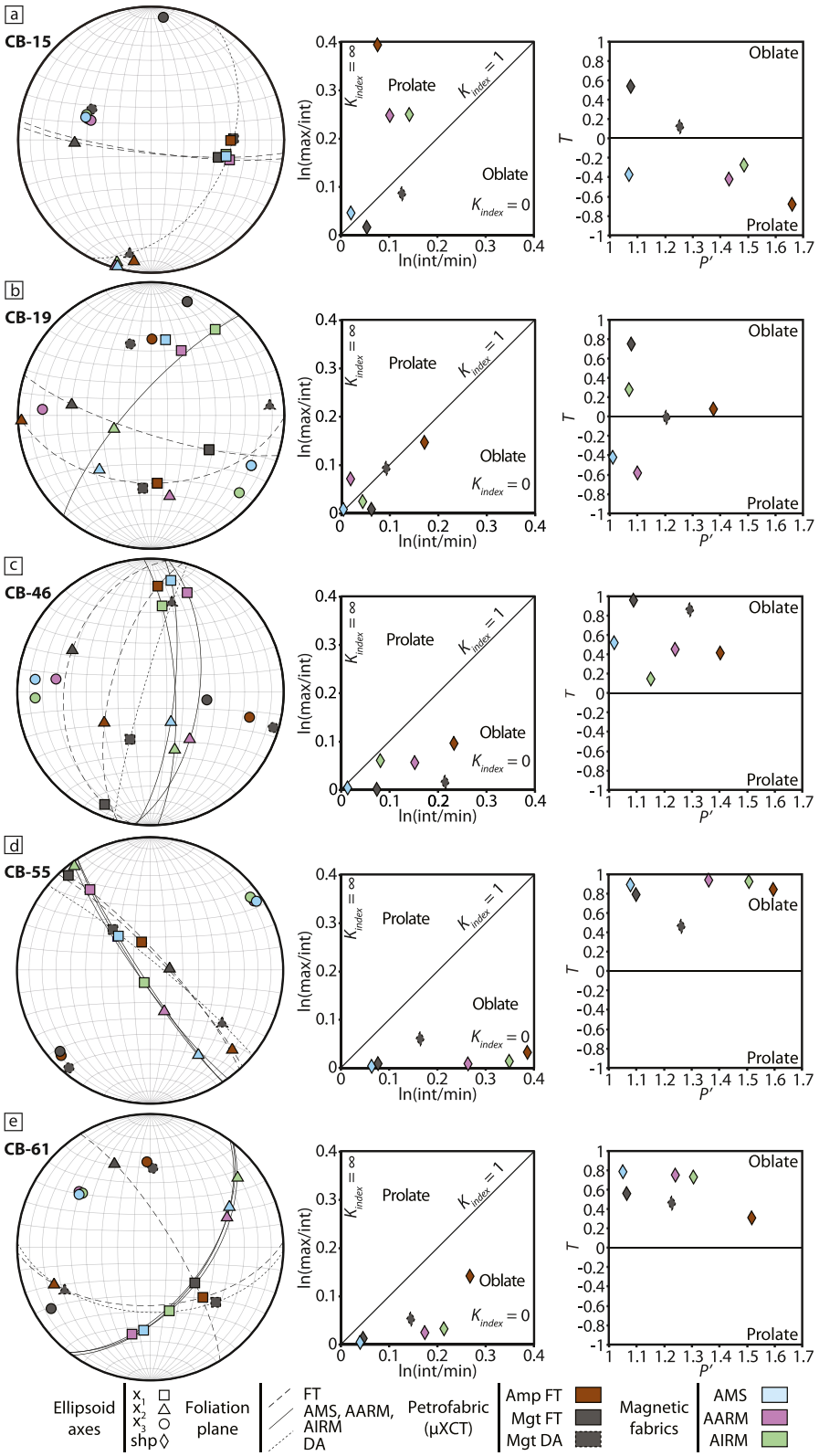
a
CB-15
b
CB-19
c
CB-46
d
CB-55
e
CB-61
ln(max/int)
ln(int/min)
Prolate
Oblate
$K_{index} = 1$
$K_{index} = 0$
$K_{index} = \infty$
T
P′
Ellipsoid axes
x_1 x_2 x_3 shp
Foliation plane
FT
AMS, AARM, AIRM
DA
Petrofabric (μXCT)
Amp FT
Mgt FT
Mgt DA
Magnetic fabrics
AMS
AARM
AIRM

AARM R_1. The AIRM fabric is transitional oblate and R_1 is co-axial to magnetite V_3 (Figure 7b). The AMS and AARM fabrics are therefore inverse relative to amphibole FT and magnetite DA, whereas the AIRM fabric is inverse relative to the magnetite FT fabric (Figure 7b). The three contrasting petrofabric components therefore seem to neutralize the AMS fabric, resulting in very low degree of anisotropy (P'). The AMS ellipsoid still reflect the analyzed components of the petrofabric, albeit the principal axes position has been flipped relative to the principal axes of the petrofabric ellipsoids.

In CB-46, the k_1, k_2 and AIRM R_1, R_2, as well as the λ_1 and λ_2 of magnetite plot along a subvertical NNE-SSW girdle (Figure 7c). The amphibole FT foliation is parallel to the AMS foliation, but dips moderately toward west and amphibole v_1 axes are clustered toward the poles of the Schmidt net (Figure 5f). The magnetite FT shows, however, a strongly oblate fabric that dips gently toward west, although with a similar strike of the foliation plane as the amphibole shape and magnetite DA fabrics (Figures 5e, 5f, 6e and 6f). The AMS signal correlates well with the magnetite spatial distribution in terms of its foliation (k_1–k_2 plane), but the k_1 orientation is in better agreement with the amphibole SPO (Figures 6e and 7c). All petrofabric elements that may contribute to the magnetic fabrics are oblate but not co-axial (Figure 7c). The misorientation of the petrofabric components results in a competition that neutralizes the AMS shape factor and lowers the degree of anisotropy. Among the three components of the petrofabric, the magnetite DA governs the AMS foliation, as indicated by their close spatial correlation. However, the orientation of the k_1 axis is clearly related to the SPO of amphibole and, to some degree, the magnetite SPO (Figure 7c).

In CB-55, the AMS k_1 and k_2, AARM and AIRM R_1 and R_2 principal axes plot along the same NW-SE oriented steeply dipping girdle as the amphibole and magnetite O_1, V_1 and O_2, V_2, whereas the AMS k_3 and AARM R_3 and the V_3, O_3 are horizontally clustered to the NE and SW (Figure 7d). Both the magnetite and the amphibole in sample CB-55 display a strong v_1 girdle distribution and the FTs yield a high shape factor (T) (Figure 5g). The AMS shape factor also indicates a strongly oblate fabric. The DA of magnetite displays an oblate shape that is coaxial to the other fabric elements (Figure 7d). The principal axes of the magnetic fabrics of sample CB-55 are therefore controlled by a combination of magnetite SPO, the magnetite spatial distribution and amphibole SPO. The concordance of the three components of the petrofabric in CB-55 accentuates both the shape parameter and degree of anisotropy.

The volume of the core processed was increased for CB-61 magnetite relative to the other samples because the magnetite petrofabric components display a large variation in fabric orientation in the different grain sizes (Figure 6i). These large variations in magnetite SPO between different grain sizes result in a relatively low degree of anisotropy for the magnetite components of the petrofabric. Magnetite FT is oblate in CB-61 with a NW-SE striking foliation (Figures 5i and 6i). The orientation of the magnetite FT foliation contrasts the magnetite DA and amphibole FT foliations, which are oriented E-W (Figure 6i and Table S3). The AMS, AARM, and AIRM ellipsoids are oblate and their foliation strikes NE-SW (Figure 7e). The magnetite DA and amphibole SPO are coaxial, whereas the magnetite SPO is oriented at right angle to the amphibole SPO and the magnetite DA foliation (Figure 7e). The AMS fabric seems to reflect the competition between the relatively weakly anisotropic magnetite DA and magnetite SPO, resulting in the misorientation relative to the analyzed components of the petrofabric (Figure 7e).

Figure 7. Lower-hemisphere equal-area Schmidt nets showing the petrofabric and magnetic fabric of the analyzed cores. Only the three components of the petrofabric that control the magnetic fabrics are shown on the plots. A foliation plane was fitted to the long (x_1) and intermediate (x_2) axis of the different fabric axes if $T > 0$. The fabric parameters calculated with the axis length of the different fabrics are plotted in Ramsay-type and Jelínek-type diagrams. (a) CB-15C2. The V_1, k_1, R_1, λ_1 plot close to each other, whereas the magnetite V_3 plot along the same girdle as the k_2 and k_3 and R_2 and R_3 anisotropy of anhysteretic remanence magnetization (AARM) and anisotropy of isothermal remanence magnetization (AIRM) principal axes. V_1 and magnetite V_1 are both located on the magnetite distribution anisotropy (DA) foliation plane, that is, they point in the direction of the plane in which magnetite grains are spatially distributed. (b) CB-19A1. k_1 and AARM R_1 plots close to amphibole V_3 and magnetite λ_3 and is inverse relative to amphibole V_1 and magnetite λ_1. The magnetite FT foliation strike parallel to the amphibole FT foliation and magnetite DA foliation, however, is more steeply inclined. Fabric parameters show that magnetite FT is oblate, whereas the AMS fabric is prolate, amphibole FT and magnetite DA are triaxial. (c) CB-46A1. The amphibole V_1 plots close to the k_1 and R_1 principal axes. The magnetite shape fabric is distinctly oblate and dips shallowly to the west and the anisotropy of magnetic susceptibility (AMS) k_1 principal axis is located on the magnetite V_1 and V_2 girdle. However, the AMS foliation is steeply dipping and is similar to the magnetite DA foliation. (d) CB-55A1. The V_1, V_2 of the amphibole and magnetite crystals population and the k_1, k_2, R_1, R_2 AMS, AIRM and AARM principal axes, as well as the magnetite λ_1 and λ_2 plot along a NW-SE girdle. All fabrics analyzed are parallel as indicated by the tightly clustered short (x_3) axes of the different fabrics. (e) CB-61B2. All fabrics are oblate as indicated by the fabric shape factors. The magnetite fabric tensor (FT) foliation plane is oriented at a right angle to the magnetite DA and amphibole FT planes. The AMS, AARM and AIRM foliation is oriented between the magnetite FT and DA foliations.

5.2. The Origin of the Magnetic Fabrics

Depending on their relative strength and orientation, the magnetite SPO and DA and amphibole SPO either constructively or destructively interfere to produce the AMS fabric in our samples. If all petrofabric elements are coaxial (CB-55), the AMS P' is relatively large and the AMS T reflects the near rotational oblate shape of the mineral shape fabric (Figure 7d). In samples where the magnetite DA and amphibole SPO are coaxial and their foliations are oriented perpendicular to the magnetite SPO foliation (CB-15 and 61) the AMS P' is also moderate to strong (Figures 7a and 7e). The distinct differences in the orientation of the petrofabric components may result in a AMS fabric dominated by some components of the petrofabric (CB-15) or magnetic fabrics that represent a mix of the components of the petrofabric (CB-61). However, when the magnetite DA, magnetite SPO and amphibole SPO foliations strike parallel, but have different inclinations (CB-19 and 46) the AMS P' is weak (Figures 7b and 7c). The competition between the components of the petrofabric may therefore neutralize the degree of anisotropy and the AMS ellipsoid shape.

The larger P' values of the AARM and AIRM tensors compared to the AMS tensor are expected and reflect magnetic anisotropies of the remanence carrying phases (cf. Jackson, 1991; McCabe et al., 1985; Stephenson et al., 1986) (Figure 7 and Table 2); the high bulk magnetic susceptibility of our samples ($>10^{-3}$ SI) and the positive correlation between AMS, AARM and low-field AIRM indicates that the AMS signal is primarily controlled by MD magnetite (Stephenson et al., 1986). Yet, the amphibole FT and AMS are largely co-axial in our samples (Figure 7). Single-amphibole-crystal AMS show that the k_1 axis may correlate with the short or intermediate axes (crystallographic a and b axis) of a amphibole crystal and hence not with the macroscopic shape fabric (long axis lineation, c axis) for amphibole of a given composition (Biedermann et al., 2015, 2018). This may hamper the direct correlation between the amphibole FT (its SPO) and AMS. However, magnetite inclusions in paramagnetic minerals have been suggested to amplify the mineral AMS signal, which is likely due to the fact that the inclusion shape reflects the shape of the host-silicate crystal and cleavage planes (Lagroix & Borradaile, 2000; Renne et al., 2002; Selkin et al., 2014). The small size of micrometer-scale magnetite inclusions (likely SD/SP grains) in amphibole alteration rims in our samples precludes any analysis of their SPO due to the resolution of our μXCT data. Yet, the AMS signal may be largely controlled by their shape and/or spatial distribution (DA), this would explain why AMS and amphibole SPO results are often coaxial when the magnetite SPO is non-coaxial. Plagioclase is the most abundant phenocryst phase in the Cerro Bayo trachyandesite and it has previously been shown that plagioclase host magnetite inclusions, which may affect the magnetic fabrics of a rock (cf. Ageeva et al., 2020; Feinberg et al., 2006). However, compared to the amphibole phenocrysts, few magnetite inclusions are observed within plagioclase phenocrysts in the Cerro Bayo samples (cf. Figure 1b); we therefore consider that the amphibole related fabrics are more likely to influence the magnetic fabrics of the samples rather than the plagioclase related fabrics.

Information on the expected SP/SD contribution to each sample's magnetic fabrics is garnered from its coercivity spectra because SD magnetite has higher coercivity than MD magnetite (Dunlop & Özdemir, 1997). CB-19 and 46 display relatively higher coercivity and require fields of 300–600 mT to achieve 95% saturation. In contrast CB-15, CB-55 and CB-61 are saturated in fields ≤300 mT (Figure S3). Together with the susceptibility temperature dependence experiments (Figures 2k–2o), these data suggest that SP/SD magnetite makes a relatively greater contribution to the magnetic fabrics of CB-19 and CB-46. Notably, the components of the MD magnetite petrofabric in CB-19 and 46 are non-coaxial (Figures 6 and 7). These components are expected to interfere destructively with each other and result in a lower degree of anisotropy. To investigate the fabric of higher coercivity grains in our samples we employed pAARM. In all samples except CB-19, the pAARM R_1 and R_2 plot along the AMS k_1-k_2 girdle (Figure S5, Table S2). The R_1 and R_2 pAARM principal directions of CB-19 plot on a NE-dipping girdle and the pAARM R_2 axes have flipped position with the AIRM and AARM R_3 axes (Figures 7b and S5). In CB-19, the magnetic fabrics are inverse relative to the three components of the petrofabric, however, the fabric is not magnetically inverse as indicated by the co-axial k_1 and AARM R_1 (Figure 7e). Hence, the AMS fabric of CB-19 is the result of the destructive interference between petrofabric components, which lowers the degree of anisotropy and causes higher coercivity magnetite grains, likely SD, to influence the position of the k_1 axis. The magnetic fabrics in CB-19 may thus be classified as intermediate fabrics (cf. Ferré, 2002), due to the competing components of the petrofabric and the MD and SD (magnetite) magnetic fabrics.

5.3. The Role of the Distribution Anisotropy

In our samples, the AMS fabric shows a clear correlation to the spatial distribution (i.e., DA) of magnetite. As previously established, the effect of the DA of magnetite on AMS becomes significant when ferrimagnetic grains are located close enough to each other to magnetically interact (Cañón-Tapia, 1996, 2001; Gaillot et al., 2006; Grégoire et al., 1995, 1998; Hargraves et al., 1991; Stephenson, 1994). The DA of amphibole, although being a fabric element that is easy to see in the field, is therefore not significant since amphibole is paramagnetic and does not interact magnetically. About 50%–60% of the magnetite crystals in the analyzed samples are located close enough to their neighbors to interact magnetically (see Section 4.1.), which validates the observed effect of the DA on the AMS ellipsoid. Our results further corroborate the results of the two-crystal experimental setup of Gaillot et al. (2006), which showed that the degree of anisotropy of AMS becomes stronger when the DA is parallel to the SPO compared to when the DA is not parallel to the SPO of magnetite crystals. The presence of discordant magnetite DA can overtake the magnetite SPO, leading to AMS sub-fabrics, a good example of this relationship is the CB-61 AMS foliation plane (Figure 7e). Notably, neither AARM nor low-field AIRM are coaxial to the magnetite FT in samples with competing magnetite components of the petrofabric (CB-15, 19, 46 and 61). Instead, they display a similar relationship to the magnetite DA as the AMS fabric. This suggests that the magnetic interaction between MD magnetite grains can also influence the AARM and AIRM fabrics.

5.4. Implications for the Interpretation of the Anisotropy of Magnetic Susceptibility Fabric

Our results indicate that if rocks include clustered magnetite grains, DA may be the dominant factor controlling AMS, even if a sample is volumetrically magnetically dominated by MD magnetite crystals. Silicate SPO may also contribute to the AMS fabric in samples with high magnetic susceptibility if SP/SD magnetite is present in mineral breakdown rims and in inclusions. In our samples, the degree of anisotropy reflects how each petrofabric component contributes to the AMS and anisotropy of remanence fabrics. Samples with relatively high degrees of anisotropy have subfabrics that constructively interfere, that is, the DA is parallel to the mineral shape fabrics (FT, OT) of the sample. In the samples with low degrees of anisotropy, different components of the petrofabric are generally non-coaxial and destructively interfere with each other. The AMS may then (a) reflect a combination of shape and DA fabrics of magnetite; (b) be dominated by one petrofabric element, but is influenced to some extent by the other sub-fabrics; or (c) be affected by SD/SP ferrimagnetic grains and result in inverse fabrics relative to the SPO and DA of MD magnetite.

6. Conclusions

In this study we investigated the source of the AMS, AARM and AIRM fabrics in the Cerro Bayo trachyandesite by using μXCT and novel and established statistical methods to analyze the petrofabric. Specifically, magnetite in the Cerro Bayo trachyandesite occurs in clusters, which makes it an ideal target to test how far DA influences the orientation and shape of the AMS, AARM and AIRM tensors in a rock dominantly carrying MD magnetite. Our results show that:

- The AMS fabric is related to three components of the petrofabric in the Cerro Bayo trachyandesite: The amphibole shape fabric, magnetite shape fabric and magnetite spatial distribution.
- The DA of magnetite may dominate the AMS, AARM and AIRM fabrics when MD magnetite is the main magnetic carrier. This indicate that clusters of magnetite that magnetically interact behave as single crystals and can bias the magnetic fabrics.
- Amphibole SPO may have a secondary effect on the AMS of the samples. The DA of SP/SD magnetite in amphibole breakdown rims and as inclusions can affect the overall AMS fabric and essentially reflects the amphibole SPO.

The quantitative information provided by μXCT, can therefore help guide the interpretation of AMS and AARM, and considerably improve the use of AMS and AARM as quantitative fabric indicators.

Conflict of Interest

The authors declare no conflicts of interest relevant to this study.

Data Availability Statement

All data sets generated for this research have been archived in the Swedish National Data Service (https://snd.gu.se/en) and can be accessed from this in-text data citation reference (Mattsson et al., 2021, https://doi.org/10.5878/qvth-zy87).

Acknowledgments
The authors are grateful for field assistance by Tobias Schmiedel, Matias Garcés and Francisco Carrera and hospitality and the help from the Sosa family and Rubén Castillo. The Swedish Geological Survey is acknowledged for access to core drilling facilities. Martin Chadima is thanked for assistance with AARM tensor element calculation. We thank Mark Dekkers for editorial handling and for helpful and constructive reviews by Ken Kodama and France Lagroix. The fieldwork was supported by the DIPS project (grant no. 240467) and the MIMES project (grant no. 244155) funded by the Norwegian Research Council awarded to O. Galland. O. Palma's position was funded from Y-TEC.

References

Ageeva, O., Bian, G., Habler, G., Pertsev, A., & Abart, R. (2020). Crystallographic and shape orientations of magnetite micro-inclusions in plagioclase. *Contributions to Mineralogy and Petrology*, *175*, 95. https://doi.org/10.1007/s00410-020-01735-8

Almqvist, B. S. G., Bosshard, S. A., Hirt, A. M., Mattsson, H. B., & Hetényi, G. (2012). Internal flow structures in columnar jointed basalt from Hrepphólar, Iceland: II. Magnetic anisotropy and rock magnetic properties. *Bulletin of Volcanology*, *74*, 1667–1681. https://doi.org/10.1007/s00445-012-0622-0

Arbaret, L., Launeau, P., Diot, H., & Sizaret, S. (2013). Magnetic and shape fabrics of magnetite in simple shear flows. *Journal of Volcanology and Geothermal Research*, *249*, 25–38. https://doi.org/10.1016/j.jvolgeores.2012.09.003

Archanjo, C. J., & Launeau, P. (2004). Magma flow inferred from preferred orientations of plagioclase of the Rio Ceará-Mirim dyke swarm (NE Brazil) and its AMS significance. *Geological Society, London, Special Publications*, *238*, 285–298. https://doi.org/10.1144/GSL.SP.2004.238.01.17

Biedermann, A. R. (2018). Magnetic anisotropy in single crystals: A review. *Geosciences*, *8*, 302. https://doi.org/10.3390/geosciences8080302

Biedermann, A. R. (2019). Magnetic pore fabrics: The role of shape and distribution anisotropy in defining the magnetic anisotropy of ferrofluid-impregnated samples. *Geochemistry, Geophysics, Geosystems*, *20*, 5650–5666. https://doi.org/10.1029/2019GC008563

Biedermann, A. R. (2020a). Current challenges and future developments in magnetic fabric research. *Tectonophysics*, *795*, 228632. https://doi.org/10.1016/j.tecto.2020.228632

Biedermann, A. R. (2020b). FinIrrSDA: A 3-D model for magnetic shape and distribution anisotropy of finite irregular arrangements of particles with different sizes, geometries, and orientations. *Journal of Geophysical Research: Solid Earth*, *125*. e2020JB020300. https://doi.org/10.1029/2020JB020300

Biedermann, A. R., Koch, C. B., Pettke, T., & Hirt, A. M. (2015). Magnetic anisotropy in natural amphibole crystals. *American Mineralogist*, *100*, 1940–1951. https://doi.org/10.2138/am-2015-5173

Biedermann, A. R., Kunze, K., & Hirt, A. M. (2018). Interpreting magnetic fabrics in amphibole-bearing rocks. *Tectonophysics*, *722*, 566–576. https://doi.org/10.1016/j.tecto.2017.11.033

Bilardello, D. (2020). Practical magnetism II: Humps and a bump, the maghemite song. *The IRM Quarterly*, *30*, 1–17.

Bilardello, D., & Jackson, M. J. (2014). A comparative study of magnetic anisotropy measurement techniques in relation to rock-magnetic properties. *Tectonophysics*, *629*, 39–54. https://doi.org/10.1016/j.tecto.2014.01.026

Bogue, S. W., Gromme, S., & Hillhouse, J. W. (1995). Paleomagnetism, magnetic anisotropy, and mid-Cretaceous paleolatitude of the Duke Island (Alaska) ultramafic complex. *Tectonics*, *14*, 1133–1152. https://doi.org/10.1029/95TC01579

Borradaile, G. J., & Jackson, M. (2010). Structural geology, petrofabrics and magnetic fabrics (AMS, AARM, AIRM). *Journal of Structural Geology*, *32*, 1519–1551. https://doi.org/10.1016/j.jsg.2009.09.006

Borradaile, G. J., & Lagroix, F. (2001). Magnetic fabrics reveal upper mantle flow fabrics in the Troodos ophiolite complex, Cyprus. *Journal of Structural Geology*, *23*, 1299–1317. https://doi.org/10.1016/S0191-8141(00)00186-3

Bouchez, J.-L. (2000). Anisotropie de susceptibilité magnétique et fabrique des granites. *Comptes Rendus de l'Académie Des Sciences - Series IIA - Earth and Planetary Science*, *330*, 1–14. https://doi.org/10.1016/S1251-8050(00)00120-8

Burchardt, S., Mattsson, T., Palma, J. O., Galland, O., Almqvist, B., Mair, K., et al. (2019). Progressive growth of the Cerro Bayo Cryptodome, Chachahuén Volcano, Argentina—Implications for viscous magma emplacement. *Journal of Geophysical Research: Solid Earth*, *124*, 7934–7961. https://doi.org/10.1029/2019JB017543

Butler, R. F., & Banerjee, S. K. (1975). Theoretical single-domain grain size range in magnetite and titanomagnetite. *Journal of Geophysical Research*, *80*, 4049–4058. https://doi.org/10.1029/JB080i029p04049

Cañón-Tapia, E. (1996). Single-grain versus distribution anisotropy: A simple three-dimensional model. *Physics of the Earth and Planetary Interiors*, *94*, 149–158. https://doi.org/10.1016/0031-9201(95)03072-7

Cañón-Tapia, E. (2001). Factors affecting the relative importance of shape and distribution anisotropy in rocks: Theory and experiments. *Tectonophysics*, *340*, 117–131. https://doi.org/10.1016/S0040-1951(01)00150-0

Cañón-Tapia, E., & Castro, J. (2004). AMS measurements on obsidian from the Inyo Domes, CA: A comparison of magnetic and mineral preferred orientation fabrics. *Journal of Volcanology and Geothermal Research*, *134*, 169–182. https://doi.org/10.1016/j.jvolgeores.2004.01.005

Chadima, M., Cajz, V., & Týcová, P. (2009). On the interpretation of normal and inverse magnetic fabric in dikes: Examples from the Eger Graben, NW Bohemian Massif. *Tectonophysics*, *466*, 47–63. https://doi.org/10.1016/j.tecto.2008.09.005

Chadima, M., Hrouda, F., & Jelínek, V. (2019). Anisoft5. Software.

Chadima, M., Pokorny, J., & Dusek, M. (2018). Rema6. Software.

Cifelli, F., Mattei, M., Chadima, M., Lenser, S., & Hirt, A. M. (2009). The magnetic fabric in "undeformed clays": AMS and neutron texture analyses from the Rif Chain (Morocco). *Tectonophysics*, *466*, 79–88. https://doi.org/10.1016/J.TECTO.2008.08.008

Coe, R. S. (1966). Analysis of magnetic shape anisotropy using second-rank tensors. *Journal of Geophysical Research*, *71*, 2637–2644. https://doi.org/10.1029/JZ071i010p02637

Di Chiara, A., Morris, A., Anderson, M. W., Menegon, L., & Tremblay, A. (2020). Magnetic anisotropy reveals Acadian transpressional fabrics in an Appalachian ophiolite (Thetford Mines, Canada). *Geophysical Journal International*, *222*, 1034–1045. https://doi.org/10.1093/gji/ggaa173

Dunlop, D. J. (1981). The rock magnetism of fine particles. *Physics of the Earth and Planetary Interiors*, *26*, 1–26. https://doi.org/10.1016/0031-9201(81)90093-5

Dunlop, D. J., & Özdemir, Ö. (1997). Rock Magnetism. Fundamentals and Frontiers, 1998/03/01. ed, Cambridge Studies in Magnetism Series XXI. Cambridge University Press, Cambridge, New York. https://doi.org/10.1017/S0016756898218437

Eriksson, P. I., Riishuus, M. S., Sigmundsson, F., & Elming, S.-Å. (2011). Magma flow directions inferred from field evidence and magnetic fabric studies of the Streitishvarf composite dike in east Iceland. *Journal of Volcanology and Geothermal Research*, *206*, 30–45. https://doi.org/10.1016/j.jvolgeores.2011.05.009

Feinberg, J. M., Harrison, R. J., Kasama, T., Dunin-Borkowski, R. E., Scott, G. R., & Renne, P. R. (2006). Effects of internal mineral structures on the magnetic remanence of silicate-hosted titanomagnetite inclusions: An electron holography study. *Journal of Geophysical Research*, *111*, B12S15. https://doi.org/10.1029/2006JB004498

Ferré, E. C. (2002). Theoretical models of intermediate and inverse AMS fabrics. *Geophysical Research Letters*, *29*, 1127. https://doi.org/10.1029/2001GL014367

Finn, D., & Coe, R. (2020). Consequences of switching field angular dependence for applications of anhysteretic remanent magnetization. *Physics of the Earth and Planetary Interiors*, *305*, 106507. https://doi.org/10.1016/j.pepi.2020.106507

Frandsen, C., Stipp, S. L. S., McEnroe, S. A., Madsen, M. B., & Knudsen, J. M. (2004). Magnetic domain structures and stray fields of individual elongated magnetite grains revealed by magnetic force microscopy (MFM). *Physics of the Earth and Planetary Interiors*, *141*, 121–129. https://doi.org/10.1016/j.pepi.2003.12.001

Gaillot, P., de Saint-Blanquat, M., & Bouchez, J.-L. (2006). Effects of magnetic interactions in anisotropy of magnetic susceptibility: Models, experiments and implications for igneous rock fabrics quantification. *Tectonophysics*, *418*, 3–19. https://doi.org/10.1016/j.tecto.2005.12.010

García-Lasanta, C., Oliva-Urcia, B., Román-Berdiel, T., Casas, A. M., & Pérez-Lorente, F. (2013). Development of magnetic fabric in sedimentary rocks: Insights from early compactional structures. *Geophysical Journal International*, *194*, 182–199. https://doi.org/10.1093/gji/ggt098

Geoffroy, L., Callot, J. P., Aubourg, C., & Moreira, M. (2002). Magnetic and plagioclase linear fabric discrepancy in dykes: A new way to define the flow vector using magnetic foliation. *Terra Nova*, *14*, 183–190. https://doi.org/10.1046/j.1365-3121.2002.00412.x

Grégoire, V., Darrozes, J., Gaillot, P., Nédélec, A., & Launeau, P. (1998). Magnetite grain shape fabric and distribution anisotropy vs rock magnetic fabric: A three-dimensional case study. *Journal of Structural Geology*, *20*, 937–944. https://doi.org/10.1016/S0191-8141(98)00022-4

Grégoire, V., de Saint Blanquat, M., Nédélec, A., & Bouchez, J.-L. (1995). Shape anisotropy versus magnetic interactions of magnetite grains: Experiments and application to AMS in granitic rocks. *Geophysical Research Letters*, *22*, 2765–2768. https://doi.org/10.1029/95GL02797

Hargraves, R. B., Johnson, D., & Chan, C. Y. (1991). Distribution anisotropy: The cause of AMS in igneous rocks? *Geophysical Research Letters*, *18*, 2193–2196. https://doi.org/10.1029/91GL01777

Hext, G. R. (1963). The estimation of second-order tensors, with related tests and designs. *Biometrika*, *50*, 353–373. https://doi.org/10.1093/biomet/50.3-4.353

Holmberg, E. (1962). Descripción geológica de la hoja 32-d, Chachahuén. Provincias de Neuquén y Mendoza, Argentina, Escala 1:200.000. Carta Geológico-Económica de la República Argentina. Boletín 91. Buenos Aires, Servicio Nacional Geológico Minero.

Hrouda, F. (1982). Magnetic anisotropy of rocks and its application in geology and geophysics. *Geophysical Surveys*, *5*, 37–82. https://doi.org/10.1007/BF01450244

Jackson, M. (1991). Anisotropy of magnetic remanence: A brief review of mineralogical sources, physical origins, and geological applications, and comparison with susceptibility anisotropy. *Pure and Applied Geophysics*, *136*, 1–28. https://doi.org/10.1007/BF00878885

Jelínek, V. (1977). The statistical theory of measuring anisotropy of magnetic susceptibility of rocks and its application. Geofyzika, Brno.

Jelínek, V. (1981). Characterization of the magnetic fabric of rocks. *Tectonophysics*, *79*, T63–T67. https://doi.org/10.1016/0040-1951(81)90110-4

Jelínek, V., & Kropáček, V. (1978). Statistical processing of anisotropy of magnetic susceptibility measured on groups of specimens. *Studia Geophysica et Geodaetica*, *22*, 50–62. https://doi.org/10.1007/BF01613632

Kay, S. M., Mancilla, O., & Copeland, P. (2006). Evolution of the late Miocene Chachahuén volcanic complex at 37°S over a transient shallow subduction zone under the Neuquén Andes. In S. M. Kay, & V. Ramos (Eds.), *Special paper 407: Evolution of an Andean margin: A tectonic and magmatic view from the Andes to the Neuquén basin (35°–39°S lat)* (pp. 215–246). Geological Society of America. https://doi.org/10.1130/2006.240710

Ketcham, R. A. (2005). Computational methods for quantitative analysis of three-dimensional features in geological specimens. *Geosphere*, *1*, 32–41. https://doi.org/10.1130/GES00001.1

Khan, M. A. (1962). The anisotropy of magnetic susceptibility of some igneous and metamorphic rocks. *Journal of Geophysical Research*, *67*, 2873–2885. https://doi.org/10.1029/JZ067i007p02873

Knight, M. D., & Walker, G. P. L. (1988). Magma flow directions in dikes of the Koolau Complex, Oahu, determined from magnetic fabric studies. *Journal of Geophysical Research*, *93*, 4301–4319. https://doi.org/10.1029/JB093iB05p04301

Lagroix, F., & Borradaile, G. J. (2000). Magnetic fabric interpretation complicated by inclusions in mafic silicates. *Tectonophysics*, *325*, 207–225. https://doi.org/10.1016/S0040-1951(00)00125-6

Lattard, D., Engelmann, R., Kontny, A., & Sauerzapf, U. (2006). Curie temperatures of synthetic titanomagnetites in the Fe-Ti-O system: Effects of composition, crystal chemistry, and thermomagnetic methods. *Journal of Geophysical Research*, *111*, B12S28. https://doi.org/10.1029/2006JB004591

Launeau, P., & Cruden, A. R. (1998). Magmatic fabric acquisition mechanisms in a syenite: Results of a combined anisotropy of magnetic susceptibility and image analysis study. *Journal of Geophysical Research*, *103*, 5067–5089. https://doi.org/10.1029/97JB02670

Martin, S. A., Kavanagh, J. L., Biggin, A. J., & Utley, J. E. P. (2019). The origin and evolution of magnetic fabrics in mafic sills. *Frontiers in Earth Science*, *7*. https://doi.org/10.3389/feart.2019.00064

Mattsson, T., Burchardt, S., Almqvist, B. S. G., & Ronchin, E. (2018). Syn-emplacement fracturing in the Sandfell laccolith, eastern Iceland—Implications for rhyolite intrusion growth and volcanic hazards. *Frontiers in Earth Science*, *6*, 5. https://doi.org/10.3389/feart.2018.00005

Mattsson, T., Petri, B., & Almqvist, B. S. G. (2021). *Data generated during the study: Decrypting magnetic fabrics (AMS, AARM, AIRM) through the analysis of mineral shape fabrics and distribution anisotropy*. Swedish National Data Service. https://doi.org/10.5878/qvth-zy87

McCabe, C., Jackson, M., & Ellwood, B. B. (1985). Magnetic anisotropy in the Trenton limestone: Results of a new technique, anisotropy of anhysteretic susceptibility. *Geophysical Research Letters*, *12*, 333–336. https://doi.org/10.1029/GL012i006p00333

McCarthy, W., Petronis, M. S., Reavy, R. J., & Stevenson, C. T. (2015a). Distinguishing diapirs from inflated plutons: An integrated rock magnetic fabric and structural study on the Roundstone Pluton, western Ireland. *Journal of the Geological Society*, *172*, 550–565. https://doi.org/10.1144/jgs2014-067

McCarthy, W., Reavy, R. J., Stevenson, C. T., & Petronis, M. S. (2015b). Late Caledonian transpression and the structural controls on pluton construction; new insights from the Omey Pluton, western Ireland. *Earth and Environmental Science Transactions of the Royal Society of Edinburgh*, *106*, 11–28. https://doi.org/10.1017/S1755691015000201

Merz, L., Almqvist, B. S. G., Grimmer, J. C., & Kontny, A. (2019). Magnetic fabric development in the Lower Seve thrust from the COSC-1 drilling, Swedish Caledonides. *Tectonophysics*, *751*, 212–228. https://doi.org/10.1016/J.TECTO.2018.12.018

Mock, A., & Jerram, D. A. (2005). Crystal size distributions (CSD) in three dimensions: Insights from the 3D reconstruction of a highly porphyritic rhyolite. *Journal of Petrology*, *46*, 1525–1541. https://doi.org/10.1093/petrology/egi024

Morgan, D. J., & Jerram, D. A. (2006). On estimating crystal shape for crystal size distribution analysis. *Journal of Volcanology and Geothermal Research*, *154*, 1–7. https://doi.org/10.1016/J.JVOLGEORES.2005.09.016

Moskowitz, B. M., Frankel, R. B., Bazylinski, D. A., Jannasch, H. W., & Lovley, D. R. (1989). A comparison of magnetite particles produced anaerobically by magnetotactic and dissimilatory iron-reducing bacteria. *Geophysical Research Letters*, *16*, 665–668. https://doi.org/10.1029/GL016i007p00665

Nørgaard Madsen, K. (2004). Angular dependence of the switching field and implications for gyromagnetic remanent magnetization in three-axis alternating-field demagnetization. *Geophysical Journal International*, *157*, 1007–1016. https://doi.org/10.1111/j.1365-246X.2004.02228.x

Özdemir, Ö., Dunlop, D. J., & Moskowitz, B. M. (1993). The effect of oxidation on the Verwey transition in magnetite. *Geophysical Research Letters*, *20*, 1671–1674. https://doi.org/10.1029/93GL01483

Payacán, I., Gutiérrez, F., Gelman, S. E., Bachmann, O., & Parada, M. Á. (2014). Comparing magnetic and magmatic fabrics to constrain the magma flow record in La Gloria pluton, central Chile. *Journal of Structural Geology*, *69*, 32–46. https://doi.org/10.1016/j.jsg.2014.09.015

Pérez, M. A., & Condat, P. (1996). Geología de La Sierra de Chachahuén, Area CNQ-23. Buenos Aires, Argentina.

Petri, B., Almqvist, B. S. G., & Pistone, M. (2020). 3D rock fabric analysis using micro-tomography: An introduction to the open-source TomoFab MATLAB code. *Computers & Geosciences*, *138*, 104444. https://doi.org/10.1016/j.cageo.2020.104444

Petronis, M. S., Driscoll, B. O., Stevenson, C. T. E., & Reavy, R. J. (2012). Controls on emplacement of the Caledonian Ross of Mull Granite , NW Scotland: Anisotropy of magnetic susceptibility and magmatic and regional structures. *The Geological Society of America Bulletin*, *124*, 906–927. https://doi.org/10.1130/B30362.1

Petronis, M. S., Hacker, D. B., Holm, D. K., Geissman, J. W., & Harlan, S. S. (2004). Magmatic flow paths and palaeomagnetism of the Miocene Stoddard Mountain laccolith, Iron Axis region, Southwestern Utah, USA. *Geological Society, London, Special Publications*, *238*, 251–283. https://doi.org/10.1144/GSL.SP.2004.238.01.16

Potter, D. K., & Stephenson, A. (1988). Single-domain particles in rocks and magnetic fabric analysis. *Geophysical Research Letters*, *15*, 1097–1100. https://doi.org/10.1029/GL015i010p01097

Renne, P. R., Scott, G. R., Glen, J. M. G., & Feinberg, J. M. (2002). Oriented inclusions of magnetite in clinopyroxene: Source of stable remanent magnetization in gabbros of the Messum Complex, Namibia. *Geochemistry, Geophysics, Geosystems*, *3*, 1–11. https://doi.org/10.1029/2002GC000319

Rochette, P., Aubourg, C., & Perrin, M. (1999). Is this magnetic fabric normal? A review and case studies in volcanic formations. *Tectonophysics*, *307*, 219–234. https://doi.org/10.1016/S0040-1951(99)00127-4

Rochette, P., Jackson, M., & Aubourg, C. (1992). Rock magnetism and the interpretation of anisotropy of magnetic susceptibility. *Reviews of Geophysics*, *30*, 209. https://doi.org/10.1029/92RG00733

Scheidegger, A. E. (1965). On the statistics of the orientation of bedding planes, grain axes, and similar sedimentological data. *U.S. Geological Society Professional Paper*, *525*, 164–167.

Schöpa, A., Floess, D., de Saint Blanquat, M., Annen, C., & Launeau, P. (2015). The relation between magnetite and silicate fabric in granitoids of the Adamello Batholith. *Tectonophysics*, *642*, 1–15. https://doi.org/10.1016/j.tecto.2014.11.022

Selkin, P. A., Gee, J. S., & Meurer, W. P. (2014). Magnetic anisotropy as a tracer of crystal accumulation and transport, Middle Banded Series, Stillwater Complex, Montana. *Tectonophysics*, *629*, 123–137. https://doi.org/10.1016/j.tecto.2014.03.028

Stephenson, A. (1994). Distribution anisotropy: Two simple models for magnetic lineation and foliation. *Physics of the Earth and Planetary Interiors*, *82*, 49–53. https://doi.org/10.1016/0031-9201(94)90101-5

Stephenson, A., Sadikun, S., & Potter, D. K. (1986). A theoretical and experimental comparison of the anisotropies of magnetic susceptibility and remanence in rocks and minerals. *Geophysical Journal International*, *84*, 185–200. https://doi.org/10.1111/j.1365-246x.1986.tb04351.x

Stevenson, C. T. E., Owens, W. H., & Hutton, D. H. W. (2007). Flow lobes in granite: The determination of magma flow direction in the Trawenagh Bay Granite, northwestern Ireland, using anisotropy of magnetic susceptibility. *The Geological Society of America Bulletin*, *119*, 1368–1386. https://doi.org/10.1130/B25970.1

Sun, Y. (2018). Magma evolution of the Cerro Bayo laccolith in the Chachahuén volcanic complex, Argentina. Dissertation. Uppsala University. Retrieved from http://urn.kb.se/resolve?urn=urn:nbn:se:uu:diva-360467

Tarling, D., & Hrouda, F. (1993). *Magnetic anisotropy of rocks* (1st ed.). Springer Netherlands.

Tauxe, L., Gee, J. S., & Staudigel, H. (1998). Flow directions in dikes from anisotropy of magnetic susceptibility data: The bootstrap way. *Journal of Geophysical Research*, *103*, 17775–17790. https://doi.org/10.1029/98JB01077

Ulrich, S., & Mainprice, D. (2005). Does cation ordering in omphacite influence development of lattice-preferred orientation? *Journal of Structural Geology*, *27*, 419–431. https://doi.org/10.1016/j.jsg.2004.11.003

Watson, G. S. (1966). The statistics of orientation data. *The Journal of Geology*, *74*, 786–797. https://doi.org/10.1086/627211

Woodcock, N. H. (1977). Specification of fabric shapes using an eigenvalue method. *The Geological Society of America Bulletin*, *88*, 1231. https://doi.org/10.1130/0016-7606(1977)88<1231:SOFSUA>2.0.CO;2

Zhu, K.-Y., Li, M.-Y., Shentu, L.-F., Shen, Z.-Y., & Yu, Y.-H. (2017). Evaluation of a small-diameter sampling method in magnetic susceptibility, AMS and X-ray CT studies and its applications to mafic microgranular enclaves (MMEs) in granite. *Journal of Volcanology and Geothermal Research*, *341*, 208–227. https://doi.org/10.1016/j.jvolgeores.2017.06.002